A. Mannarino, E.H. Dowell, P. Mantegazza
An Adaptive Controller for Nonlinear Flutter Suppression and Free-Play Compensation
Journal of Vibration and Control, Vol. 23, N. 14, 2017, p. 2269-2290
doi:10.1177/1077546315613935

Journal of Vibration and Control
xxx(xx):1–33

DOI:doi number
http://mms.sagepub.com

An adaptive controller for nonlinear flutter suppression and free-play compensation

Andrea Mannarino *
Ph.D. Candidate, Dipartimento di Scienze e Tecnologie Aerospaziali, Politecnico di Milano, Via La Masa 34, 20156 Milano, Italy.

Earl H. Dowell
William Holland Hall Professor, Department of Mechanical Engineering and Materials Science; Dean Emeritus, Pratt School of Engineering, Duke University, 100 Science Dr, Durham, North Carolina 27708-0300, USA.

Paolo Mantegazza
Professor, Dipartimento di Scienze e Tecnologie Aerospaziali, Politecnico di Milano, Via La Masa 34, 20156 Milano, Italy.

Abstract

A technique aimed at neutralizing the presence of free-play effects in a control surface actuation chain is presented. It is based on an adaptive inversion of a function approximating such a nonlinearity. A simple, yet robust, on-line adaptive algorithm is proposed to identify the free-play parameters, i.e. free-play width, the equivalent control stiffness and friction.

* Corresponding author; e-mail: andrea.mannarino@polimi.it

The procedure is then coupled to an Immersion and Invariance control law to drastically reduce possible residual closed loop limit cycle oscillations due to the free-play nonlinearity. Within such a framework, the so chosen compensation technique can be interpreted as a control augmentation, easily extendable to multiple control surfaces.

The methodology is then verified on a four degree-of-freedom airfoil in transonic regime, characterized by highly nonlinear unsteady aerodynamic loads, producing significant shock motions and large limit cycles, at a relatively high frequency. The presence of both aerodynamic and structural nonlinearities makes such a system bistable, leading to complex responses dependent on the initial conditions and the input used to excite the system. The effective suppression of these auto-induced vibrations becomes even more challenging because the limit cycle oscillations generated by different sources are characterized by differing amplitudes and frequencies.

Keywords

Nonlinear aeroservoelasticity, limit cycle oscillations, reduced order models, adaptive control, free-play compensation

Nomenclature

$\mathbf{x}_{\text{a}}$	Aerodynamic state
$\mathbf{x}_{\text{s}}$	Structural dynamics state
$\mathbf{A}$, $\mathbf{B}_a$, $\mathbf{B}_c$, $\mathbf{C}_y$	State space matrices implemented in the controller
$\mathbf{A}_r$, $\mathbf{B}_{a,r}$, $\mathbf{B}_{m,r}$, $\mathbf{B}_{c,r}$, $\mathbf{C}_{y,r}$	State space matrices of the verification model
$\mathbf{z}_\beta$, $\mathbf{z}_m$, $\mathbf{z}_{\text{act}}$	Sensors output
$\mathbf{A}_{\text{ae}}$, $\mathbf{B}_{\text{ae}}$, $\mathbf{C}_{\text{ae}}$, $\mathbf{D}_{\text{ae}}$, $\mathbf{E}_{\text{ae}}$, $\mathbf{F}_{\text{ae}}$	Aerodynamic reduced order model matrices
$\boldsymbol{\phi}(\mathbf{x}_{\text{a}})$	Nonlinear terms of the aerodynamic reduced order model
$q_\infty = \frac{1}{2}\rho_\infty U_\infty^2$	Dynamic pressure
h, θ	Plunge and pitch degrees of freedom
β_{LE}, β_{TE}	Leading and trailing edge control surfaces deflection
N_a	Number of aerodynamic states, size of $\mathbf{x}_{\text{a}}$
N_{in}	Number of control input, size of $\boldsymbol{\beta}_c$
ω	Natural frequency, rad/s
$V_{\infty,\text{bif}}$	Bifurcation speed, m/s
f_{bif}	Bifurcation frequency, Hz
$\mathbf{q}_s$	Generalized structural degrees of freedom
$\mathbf{f}_a$	Generalized aerodynamic loads
$\mathbf{m}_\beta, \mathbf{m}_f$	Hinge and friction torque, Nm
$k_\beta, \beta_{\text{FP}}$	Free-play parameters
$\Delta\boldsymbol{\beta}$	Aileron dynamic response, rad

$\hat{\mathbf{m}}_f$	Friction amplitude, Nm
$\boldsymbol{\beta}_c$	Control input, rad
$\mathbf{t}$	Control design target
$\tilde{\mathbf{y}}$	Controlled performance
$\mathbf{H}$	Performance output matrix
$\boldsymbol{\Lambda}, \mathbf{C}_t, \mu, \gamma_{\text{Con}}, \eta_{\text{Con}}$	Parameters of the Immersion and Invariance controller
$\mathbf{z}$	Off-the-manifold variable
$\hat{\boldsymbol{\chi}}$	Immersion and invariance uncertain parameter vector
$\boldsymbol{\psi}$	Immersion and invariance controller regressor
$\boldsymbol{\delta}$	Immersion and invariance shaping function
$\boldsymbol{\theta}$	Approximate hinge torque parameters
η^{GD}	Learning rate of the free-play compensation algorithm
ξ	Damping ratio

Subscript

o	Variable reconstructed by the observer
f	Filtered quantity
r	Real system

1. Introduction

The study of nonlinearities in control surface actuation systems is more and more relevant in active aeroelastic control design. Therefore, an earlier introduction of nonlinear effects may lead to improved and less expensive products (Karpel et al. 2013).

Free-play nonlinearities are not only encountered in aeroservoelasticity, e.g. see the works of Karpel (Karpel et al. 2013, Gold & Karpel 2008) and Vasconcellos (Vasconcellos et al. 2014) regarding the modeling of nonlinear actuators and the series of tests recently carried out by Kholodar (Kholodar 2014). In fact they must be studied, modeled and compensated in most electro-fluid-mechanical applications (Nordin & Gutman 2002, Tao 2003, Selmic & Lewis 2000, Aghababa & Aghababa 2014, Boulkroune & M'saad 2012, Chung-Chun et al. 2008). A significant improved comprehension of free-play phenomena in control surface mechanisms can be found in the researches carried out at Duke University by Conner et al. (Conner et al. 1997b, 1996, 1997a)., similar studies being still underway on more complex models (Tang & Dowell 2013). Limit Cycle Oscillations (LCO) induced by a control surface free-play have also been studied on an F-16 aeroelastic

model (Chen & Lee 2008), simulating the effects of various free-play angles and different maneuver conditions. The same type of problems has also been experienced on real aircraft, as witnessed by (Croft 27 August 2001)

Nevertheless, the above mentioned works aimed mainly at the analysis of such peculiar nonlinear behaviors, often without addressing the possibility of compensating it. It is well known that the presence of free-play can significatively alter the stability characteristics of an aeroservoelastic system, both in open and closed loop (Gold & Karpel 2008, Huang et al. 2013). In particular, several studies have shown that the presence of such a nonlinearity can jeopardize the properties of a control law designed without accounting for it, thus leading to closed loop responses characterized by residual LCOs (Huang et al. 2013, Bae et al. 2002, Dimitriadis & Cooper 2000, Frampton & Clark 2000). Therefore, the presence of free-play often worsen the performance of aeroelastic control systems, possibly leading to multistable behaviors as in the test case considered in this work.

Following the work presented in (Mannarino & Mantegazza 2014a), the problem of the compensation of control surfaces free-play is here addressed. At first, the proposed approach designs an adaptive control law, based on the Immersion and Invariance (I&I) methodology (Astolfi et al. 2008a,b, Lee & Singh 2009), on the ideal system, i.e. by neglecting the presence of the free-play. Then, an additional adaptive control based on the nonlinear inversion approach (Tao 2003) is applied in order to compute the variation of the control input required to avoid being caught within the free-play range. To obtain such a beneficial behavior, the additional measures required are the control surface deflection, the applied torque and the actuators position, which are added to the accelerometric measures used to reconstruct the entire state by means of a sliding mode observer (Drakunov & Utkin 1995, Mannarino & Mantegazza 2014a). Within such an approach, the free-play parameters are assumed as unknown and a real time approximator can be trained on-line to estimate their values in discrete time, so to obtain a digital compensation scheme to be directly applied to realistic control problems. The proposed method will be tested on a four degrees of freedom airfoil, including strong transonic nonlinearities, taken into account through a Computational Fluid Dynamics (CFD)-based reduced order model (Mannarino & Mantegazza 2014b). This case is thus characterized by highly nonlinear unsteady aerodynamic loads, producing significant shock motions and large amplitude LCOs at a relatively high frequency, which, being coupled to a nonlinear actuation servo-system, can result in a challenging test for the proposed approach.

This work takes the basic ideas from (Mannarino 2015), but the approach is extended here to the suppression of instabilities with multiple control surfaces. As shown in Section 4, the I&I control methodology for multiple-input multiple-output systems differs significantly with respect to its single-input counterpart. Additional original contributions of this work are the introduction of a simple estimator of the possible friction torque acting on the control surfaces hinge, which further helps the reduction of the residual limit cycle oscillations, and an in-depth analysis of the influence of the actuators bandwidth on the controller performance. Furthermore, the presence of both aerodynamic and structural nonlinearities makes the system bistable, leading to complex responses dependent on the initial conditions and the input used to excite the system. To the authors' knowledge, this is one of the first studies of bistable behavior for this kind of aeroelastic and

aeroservoelastic system, even if investigations about this phenomenon were already carried out in the field of mechanics (Daynes et al. 2009) and control (Johnson et al. 2014). It makes the design of the flutter suppression system more challenging, because of the presence of different nonlinear sources, which leads to the suppression of responses characterized by a wide range of amplitudes. Although beyond the scope of this paper, a complete study of such bistable behavior is currently under investigation by the authors.

Therefore, the goal of the present paper is to demonstrate a simple yet effective method for compensating free-play nonlinearities in control systems, while also considering other kinds of nonlinear effects, e.g. shock wave aerodynamics and structural friction. In what follows, several analyses are carried out considering different values of free-play amplitudes and other key parameters, showing significant changes of the system response when they are varied. The adaptive control law is further tested against significantly modified structural parameters, highlighting a few interesting results.

2. Aeroservoelastic modeling

An aeroservoelastic system is typically composed by three interconnected parts: structure, aerodynamics and control, and, depending on specific analysis and design needs, different model fidelities can be used in the various stages of its development.

Let us breakdown our design approach, describing the design and verification models separately.

2.1. Design model

Following a standard approach, a generic linear(ized) structural model, can be discretized into the classical multi-degrees of freedom scheme:

$$\mathbf{M}_s\ddot{\mathbf{q}}_s + \mathbf{C}_s\dot{\mathbf{q}}_s + \mathbf{K}_s\mathbf{q}_s = q_\infty \mathbf{f}_\mathrm{a} + \mathbf{T}_\beta^\mathrm{T}\mathbf{m}_h \tag{1}$$

where: $\mathbf{M}_s$, $\mathbf{C}_s$, $\mathbf{K}_s$ are the structural mass, damping and stiffness matrices, $\mathbf{q}_s$ the generalized structural coordinates, whose physical meaning is determined by the assumed discretization and $\mathbf{f}_\mathrm{a}$ the external generalized aerodynamic forces, scaled by the asymptotic dynamic pressure q_∞.

To explain the term $\mathbf{T}_\beta^\mathrm{T}\mathbf{m}_h$ in the above formula, it is remarked that the degree of freedom of any control surface is typically embedded in $\mathbf{q}_s$, so to be easily interfaced to the aerodynamic subsystem in the very same way as any other structural motion. Therefore, control surface rotations, $\boldsymbol{\beta}$, will be defined by $\boldsymbol{\beta} = \mathbf{T}_\beta\mathbf{q}_s$, $\mathbf{T}_\beta$ being an appropriate kinematic linking matrix, which linearly combines the generalized coordinates $\mathbf{q}_s$ to extract the physical rotation of the movable surfaces. Through the principal of virtual work, the generalized hinge moments, $\mathbf{m}_h$, associated to the external control moments $\mathbf{m}_\beta$ and to its friction $\mathbf{m}_f$, will be given by $\mathbf{m}_h = \mathbf{T}_\beta^\mathrm{T}(\mathbf{m}_\beta + \mathbf{m}_f)$. In general, the friction torque will depend on the control surface control moments and rotation rates $\dot{\boldsymbol{\beta}}$, i.e. $\mathbf{m}_\mathrm{f} = \mathbf{m}_\mathrm{f}\left(\mathbf{m}_\beta, \mathbf{T}_{\dot\beta}\dot{\boldsymbol{\beta}}\right)$.

A sample free-play behavior is shown in Figure 1. The related mathematical model for each control surface can be described as follows:

$$m_\beta = \begin{cases} k_\beta \left(\Delta\beta + \beta_{\text{FP}}\right) & \text{for} \quad \Delta\beta < -\beta_{\text{FP}} \\ 0 & \text{for} \quad |\Delta\beta| < \beta_{\text{FP}} \\ k_\beta \left(\Delta\beta - \beta_{\text{FP}}\right) & \text{for} \quad \Delta\beta > \beta_{\text{FP}} \end{cases} \tag{2}$$

$$\Delta\beta = \beta_{\text{ext}} + \beta_c - \beta$$

The variable $\Delta\beta$ is often referred as aileron dynamic response (Gold & Karpel 2008) and it can be decomposed into three contributions: β_{ext} is the applied external command, β_c the command computed by some control logic and β the effective aileron deflection. In addition, k_β is the equivalent stiffness connecting the pilot command to the control surface and β_{FP} is the semi-width of the free-play, here assumed symmetric. As clarified in the following, the friction torque will be modeled

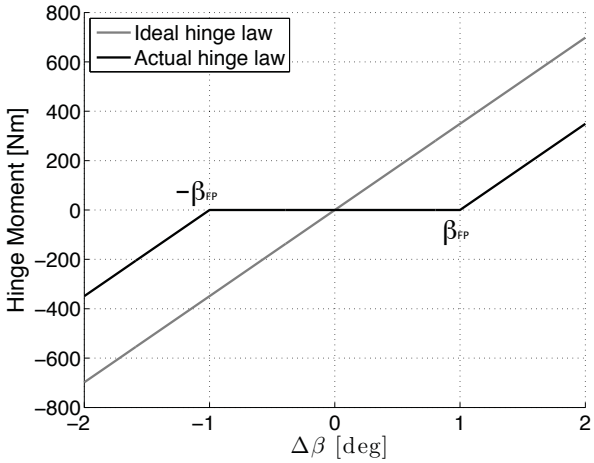

Fig. 1. Comparison between ideal and actual hinge moment

differently in the computational model used by the controller and in the actual plant under control. In fact, as it will be seen later on, the controller considers a simple averaged Coloumb like approximation, of the kind $m_f = \hat{m}_f \text{sign}\left(\dot{\beta}\right)$, $\hat{m}_f$ being a percentage of the maximum torque transmitted by the actuator, while a more elaborate Stribeck formulation (Ferretti et al. 2003) will be used for a more accurate system simulation.

In view of the need of modeling the transfer function of the accelerometer based measures required by the state observer, the related acceleration output, at assigned locations, will be given by $\mathbf{a} = \mathbf{T}_a \ddot{\mathbf{q}}_s$, $\mathbf{T}_a$ being a suitable displacement interpolation matrix, which linearly combines the accelerations of the generalized degrees of freedom to obtain the accelerations at any point of the structure. Therefore, after defining with $\mathcal{D}(\mathbf{v})$ the diagonal matrix associated to a vector $\mathbf{v}$, the related transducer dynamics is approximated through:

$$\ddot{\mathbf{z}}_{\text{acc}} + \mathcal{D}(2\xi_{\text{acc}}\omega_{\text{acc}})\dot{\mathbf{z}}_{\text{acc}} + \mathcal{D}(\omega_{\text{acc}}^2)\mathbf{z}_{\text{acc}} = \mathcal{D}(\omega_{\text{acc}}^2)\mathbf{a} = \mathcal{D}(\omega_{\text{acc}}^2)\mathbf{T}_a\ddot{\mathbf{q}}_s \tag{3}$$

Similarly, the measures of control surfaces deflection and applied torques are simulated by means of second order transfer functions:

$$\ddot{\mathbf{z}}_\beta + \mathcal{D}(2\xi_{\text{sens}}\omega_{\text{sens}})\dot{\mathbf{z}}_\beta + \mathcal{D}(\omega_{\text{sens}}^2)\mathbf{z}_\beta = \mathcal{D}(\omega_{\text{sens}}^2)\boldsymbol{\beta} = \mathcal{D}(\omega_{\text{sens}}^2)\mathbf{T}_\beta\mathbf{q}_s \tag{4a}$$

$$\ddot{\mathbf{z}}_m + \mathcal{D}(2\xi_{\text{sens}}\omega_{\text{sens}})\dot{\mathbf{z}}_m + \mathcal{D}(\omega_{\text{sens}}^2)\mathbf{z}_m = \mathcal{D}(\omega_{\text{sens}}^2)\left(\mathbf{m}_\beta + \mathbf{m}_f\right) \tag{4b}$$

It should be remarked from Eq. 4b that the hinge torque measure cannot separate the contributions of free-play and friction. Finally, a generic formulation of a nonlinear unsteady aerodynamic system is written as:

$$\begin{cases} \dot{\mathbf{x}}_a &= \mathbf{f}_{x_a}\left(\mathbf{x}_a, \mathbf{q}_s, \dot{\mathbf{q}}_s\right) \\ \mathbf{f}_a &= \mathbf{f}_a\left(\mathbf{x}_a, \mathbf{q}_s, \dot{\mathbf{q}}_s\right) \end{cases} \tag{5}$$

where $\mathbf{x}_a$ is the aerodynamic state, which can be either a physical entity, as in the case of a raw CFD model, or a generically abstract reduced order state.

Defining the extended servo-elasto-mechanical degrees of freedom $\mathbf{q} = \left[\mathbf{q}_s\ \mathbf{z}_{\text{acc}}\ \mathbf{z}_\beta\ \mathbf{z}_m\right]^{\text{T}}$ and the corresponding state $\mathbf{x} = \left[\mathbf{q}\ \dot{\mathbf{q}}\right]^{\text{T}} = \left[\mathbf{q}_s\ \mathbf{z}_{\text{acc}}\ \mathbf{z}_\beta\ \mathbf{z}_m\ \dot{\mathbf{q}}_s\ \dot{\mathbf{z}}_{\text{acc}}\ \dot{\mathbf{z}}_\beta\ \dot{\mathbf{z}}_m\right]^{\text{T}}$, putting together all of what above, the following nonlinear, strictly proper, state space formulation is obtained:

$$\begin{cases} \dot{\mathbf{x}} &= \mathbf{A}\mathbf{x} + q_\infty\mathbf{B}_a\,\mathbf{f}_a\left(\mathbf{x}_a, \mathbf{q}_s, \dot{\mathbf{q}}_s\right) + \mathbf{B}_c\mathbf{m}_f + \mathbf{B}_c\mathbf{m}_\beta \\ \dot{\mathbf{x}}_a &= \mathbf{f}_{x_a}\left(\mathbf{x}_a, \mathbf{q}_s, \dot{\mathbf{q}}_s\right) \\ \mathbf{y} &= \mathbf{C}_y\mathbf{x} \end{cases} \tag{6}$$

where $\mathbf{y}$ is the system output and the other terms are defined through the following intermediate vectors and matrices:

$$\mathbf{M} = \begin{bmatrix} \mathbf{M}_s & \mathbf{0} & \mathbf{0} & \mathbf{0} \\ -\mathcal{D}(\omega_{\text{acc}}^2)\mathbf{T}_a & \mathbf{I} & \mathbf{0} & \mathbf{0} \\ \mathbf{0} & \mathbf{0} & \mathbf{I} & \mathbf{0} \\ \mathbf{0} & \mathbf{0} & \mathbf{0} & \mathbf{I} \end{bmatrix} \quad \mathbf{C} = \begin{bmatrix} \mathbf{C}_s & \mathbf{0} & \mathbf{0} & \mathbf{0} \\ \mathbf{0} & \mathcal{D}(2\xi_{\text{acc}}\omega_{\text{acc}}) & \mathbf{0} & \mathbf{0} \\ \mathbf{0} & \mathbf{0} & \mathcal{D}(2\xi_{\text{sens}}\omega_{\text{sens}}) & \mathbf{0} \\ \mathbf{0} & \mathbf{0} & \mathbf{0} & \mathcal{D}(2\xi_{\text{sens}}\omega_{\text{sens}}) \end{bmatrix} \tag{7}$$

$$\mathbf{K} = \begin{bmatrix} \mathbf{K}_s & \mathbf{0} & \mathbf{0} & \mathbf{0} \\ \mathbf{0} & \mathcal{D}(\omega_{\text{acc}}^2) & \mathbf{0} & \mathbf{0} \\ -\mathcal{D}(\omega_{\text{sens}}^2)\mathbf{T}_\beta & \mathbf{0} & \mathcal{D}(\omega_{\text{sens}}^2) & \mathbf{0} \\ \mathbf{0} & \mathbf{0} & \mathbf{0} & \mathcal{D}(\omega_{\text{sens}}^2) \end{bmatrix} \quad \mathbf{B}_{aq} = \begin{bmatrix} \mathbf{I} \\ \mathbf{0} \\ \mathbf{0} \\ \mathbf{0} \end{bmatrix} \quad \mathbf{B}_{cq} = \begin{bmatrix} \mathbf{T}_\beta^{\text{T}} \\ \mathbf{0} \\ \mathbf{0} \\ \mathcal{D}(\omega_{\text{sens}}^2) \end{bmatrix} \tag{8}$$

so that it is possible to set the following final compact elements of Eq. 6:

$$\mathbf{A} = \begin{bmatrix} \mathbf{0} & \mathbf{I} \\ -\mathbf{M}^{-1}\mathbf{K} & -\mathbf{M}^{-1}\mathbf{C} \end{bmatrix} \quad \mathbf{B}_a = \begin{bmatrix} \mathbf{0} \\ \mathbf{M}^{-1}\mathbf{B}_{aq} \end{bmatrix} \quad \mathbf{B}_c = \begin{bmatrix} \mathbf{0} \\ \mathbf{M}^{-1}\mathbf{B}_{cq} \end{bmatrix} \tag{9}$$

$$\mathbf{C}_y = \begin{bmatrix} \mathbf{0} & \mathbf{I} & \mathbf{0} & \mathbf{0} & \mathbf{0} & \mathbf{0} & \mathbf{0} & \mathbf{0} \\ \mathbf{0} & \mathbf{0} & \mathbf{I} & \mathbf{0} & \mathbf{0} & \mathbf{0} & \mathbf{0} & \mathbf{0} \\ \mathbf{0} & \mathbf{0} & \mathbf{0} & \mathbf{I} & \mathbf{0} & \mathbf{0} & \mathbf{0} & \mathbf{0} \end{bmatrix} \tag{10}$$

2.2. A comment on the design of the flutter suppression system

It should be remarked from now that the baseline I&I controller, responsible of the suppression of large amplitude limit cycle oscillations, is designed on the ideal system only, i.e. $\beta_{\text{FP}} = 0$, and considers a slightly different model than Eq. 6. In fact, discarding the free-play effect, the ideal system dynamics is governed by:

$$\begin{cases} \dot{\mathbf{x}} &= \mathbf{A}\mathbf{x} + q_\infty \mathbf{B}_a \, \mathbf{f}_a \left(\mathbf{x}_a, \mathbf{q}_s, \dot{\mathbf{q}}_s \right) + \mathbf{B}_d \mathbf{m}_f + \mathbf{B}_{c_{I\&I}} \boldsymbol{\beta}_c \\ \dot{\mathbf{x}}_a &= \mathbf{f}_{x_a} \left(\mathbf{x}_a, \mathbf{q}_s, \dot{\mathbf{q}}_s \right) \\ \mathbf{y} &= \mathbf{C}_y \mathbf{x} \end{cases} \tag{11}$$

where the matrix $\mathbf{B}_d$ has the same definition of $\mathbf{B}_c$ in Eq. 9, while $\mathbf{B}_{c_{I\&I}}$ is defined as:

$$\mathbf{B}_{c_{I\&I}} = \begin{bmatrix} \mathbf{0} \\ \mathbf{M}^{-1} \begin{bmatrix} \mathbf{T}_\beta^{\text{T}} \mathcal{D}(\mathbf{k}_\beta) \\ \mathbf{0} \\ \mathbf{0} \\ \mathcal{D}(\omega_{\text{sens}}^2) \end{bmatrix} \end{bmatrix} \tag{12}$$

Therefore the ideal controller will be designed directly on the control surfaces deflections. The vector $\mathbf{k}_\beta$ in Eq. 12 contains the nominal stiffness at each aileron hinge. With the formulation of Eq. 11, a design based directly on the controlled surface deflections $\boldsymbol{\beta}_c$ will be possible, and this result will be used as baseline by the proposed free-play compensation.

2.3. Verification model

It is important to remark that the actuator dynamics should be neglected in the controller computational model, because, as shown in Section 5, its presence would not permit the explicit inversion of the free-play nonlinearity. Nevertheless, suitable actuator models are included in the controlled system during the simulation of the controller gains tuning, thus better matching the true closed loop operation in flight.

Therefore, the often used second order transfer function (Brenner 1996) of the following type will be adopted:

$$\ddot{\mathbf{z}}_{\text{act}} + \mathcal{D}(2\xi_{\text{act}}\omega_{\text{act}})\dot{\mathbf{z}}_{\text{act}} + \mathcal{D}(\omega_{\text{act}}^2)\mathbf{z}_{\text{act}} = \mathcal{D}(\omega_{\text{act}}^2)\boldsymbol{\beta}_c \tag{13}$$

The true free-play is thus experienced between the actual actuator and aileron positions, i.e. β_c has to be substituted with z_{act} in Eq. 2. The real aeroservoelastic system under control is thus described by a set of ordinary differential equations, similar to Eq. 6, albeit with a different internal structure because of the accounted the actuator dynamics. Defining the real servoelastic state $\mathbf{x}_r = [\mathbf{q}\ \dot{\mathbf{q}}]^{\text{T}} = [\mathbf{q}_s\ \mathbf{z}_{\text{acc}}\ \mathbf{z}_\beta\ \mathbf{z}_m\ \mathbf{z}_{\text{act}}\ \dot{\mathbf{q}}_s\ \dot{\mathbf{z}}_{\text{acc}}\ \dot{\mathbf{z}}_\beta\ \dot{\mathbf{z}}_m\ \dot{\mathbf{z}}_{\text{act}}]^{\text{T}}$, the final set of equations describing the system dynamics is so modified:

$$\mathbf{M}_r = \begin{bmatrix} \mathbf{M} & \mathbf{0} \\ \mathbf{0} & \mathbf{I} \end{bmatrix} \quad \mathbf{C}_r = \begin{bmatrix} \mathbf{C} & \mathbf{0} \\ \mathbf{0} & \mathcal{D}(2\xi_{\text{act}}\omega_{\text{act}}) \end{bmatrix} \quad \mathbf{K}_r = \begin{bmatrix} \mathbf{K} & \mathbf{0} \\ \mathbf{0} & \mathcal{D}(\omega_{\text{act}}^2) \end{bmatrix} \tag{14}$$

$$\mathbf{B}_{aq,r} = \begin{bmatrix} \mathbf{I} \\ \mathbf{0} \\ \mathbf{0} \\ \mathbf{0} \\ \mathbf{0} \end{bmatrix} \quad \mathbf{B}_{mq,r} = \begin{bmatrix} \mathbf{T}_\beta^{\text{T}} \\ \mathbf{0} \\ \mathbf{0} \\ \mathcal{D}(\omega_{\text{sens}}^2) \\ \mathbf{0} \end{bmatrix} \quad \mathbf{B}_{cq,r} = \begin{bmatrix} \mathbf{0} \\ \mathbf{0} \\ \mathbf{0} \\ \mathbf{0} \\ \mathcal{D}(\omega_{\text{act}}^2) \end{bmatrix} \tag{15}$$

$$\mathbf{A}_r = \begin{bmatrix} \mathbf{0} & \mathbf{I} \\ -\mathbf{M}_r^{-1}\mathbf{K}_r & -\mathbf{M}_r^{-1}\mathbf{C}_r \end{bmatrix} \quad \mathbf{B}_{a,r} = \begin{bmatrix} \mathbf{0} \\ \mathbf{M}_r^{-1}\mathbf{B}_{aq,r} \end{bmatrix} \quad \mathbf{B}_{m,r} = \begin{bmatrix} \mathbf{0} \\ \mathbf{M}_r^{-1}\mathbf{B}_{mq,r} \end{bmatrix} \quad \mathbf{B}_{c,r} = \begin{bmatrix} \mathbf{0} \\ \mathbf{M}_r^{-1}\mathbf{B}_{cq,r} \end{bmatrix} \tag{16}$$

Leading to the following dynamic system:

$$\begin{cases} \dot{\mathbf{x}}_r &= \mathbf{A}_r\mathbf{x}_r + q_\infty\mathbf{B}_{a,r}\,\mathbf{f}_a\left(\mathbf{x}_a, \mathbf{q}_s, \dot{\mathbf{q}}_s\right) + \mathbf{B}_{m,r}\mathbf{m}_f + \mathbf{B}_{m,r}\mathbf{m}_\beta + \mathbf{B}_{c,r}\boldsymbol{\beta}_c \\ \dot{\mathbf{x}}_a &= \mathbf{f}_{x_a}\left(\mathbf{x}_a, \mathbf{q}_s, \dot{\mathbf{q}}_s\right) \\ \mathbf{y}_r &= \mathbf{C}_{y,r}\mathbf{x}_r \end{cases} \tag{17}$$

with the output equation now including also the measure of the actuator position:

$$\mathbf{C}_{y,r} = \begin{bmatrix} \mathbf{0} & \mathbf{I} & \mathbf{0} & \mathbf{0} & \mathbf{0} & \mathbf{0} & \mathbf{0} & \mathbf{0} & \mathbf{0} & \mathbf{0} \\ \mathbf{0} & \mathbf{0} & \mathbf{I} & \mathbf{0} & \mathbf{0} & \mathbf{0} & \mathbf{0} & \mathbf{0} & \mathbf{0} & \mathbf{0} \\ \mathbf{0} & \mathbf{0} & \mathbf{0} & \mathbf{I} & \mathbf{0} & \mathbf{0} & \mathbf{0} & \mathbf{0} & \mathbf{0} & \mathbf{0} \\ \mathbf{0} & \mathbf{0} & \mathbf{0} & \mathbf{0} & \mathbf{I} & \mathbf{0} & \mathbf{0} & \mathbf{0} & \mathbf{0} & \mathbf{0} \end{bmatrix} \tag{18}$$

Finally, it should also be remarked that when high fidelity aerodynamic models are taken into account, $\mathbf{x}_a$ can be very large, so that the system size can be limited substantially only by using a compact description of the aerodynamics. Therefore, whenever a high fidelity aerodynamic implies tens to hundreds of thousands states, the controller will be designed on the base of a significantly more favourable reduced order model size.

3. A few details of the aerodynamic models

Since aerodynamic phenomena will strongly affect the presented results, some details about their formulation are provided here.

3.1. CFD modeling

The aerodynamic sub-system is modeled through a cell centered finite volume scheme, using the aerodynamic code AeroFoam, developed at Dipartimento di Scienze e Tecnologie Aerospaziali, Politecnico di Milano (Romanelli et al. 2010). AeroFoam is a density-based compressible Unsteady Euler/Reynolds-Averaged-Navier-Stokes solver, the Euler option being selected in this work. Among its features there is an aeroelastic interfacing scheme, based on a moving least square interpolation strategy, providing all the needed functionalities to set the appropriate aerodynamic boundary conditions imposed by a deforming structure, while driving a connected hierarchical mesh deformation within an Arbitrary Lagrangian Eulerian formulation. An extended illustration of its aeroelastic capabilities can be found in (Romanelli et al. 2012). In this work any of AeroFoam aerodynamic formulations can be synthesized in the form of Eq. 5, with $\mathbf{x}_a$ being the physical state associated to the cell centers, i.e. density, momentum, energy and the turbulence model own state. The generalized aerodynamic loads are computed through the integration of the pressure and viscous stresses at the body surface. The high number of states (from tens of thousands to millions) required for an accurate approximation implies highly time demanding CFD-based analyses. Consequently, such simulations are mostly restricted to the verification phase of a design.

3.2. Reduced order modeling

For classical linear(ized) flows, mostly based on the solution of an integral equation, linear identification methods can be exploited to provide a reduced order state space representation, see (Ripepi & Mantegazza 2013) and references therein. Even when the flow is nonlinear, e.g. Euler-based CFD codes, linear load identification methods can be adopted for small motions around a steady trimmed solution (Hall et al. 2000). Nevertheless, when the structural system undergoes large enough motions, causing significant changes of the flow field, e.g. moving shocks, an unsteady, nonlinear aerodynamic model of the type previously described is required. As already remarked, it can provide a high level of fidelity only at the cost of a significantly fine discretization, with the related demand of computational power and time consuming simulations. This fact limits its applicability to control designs, sensitivity studies and system optimization, for which Reduced Order Models

(ROMs) are almost compulsory (Lucia et al. 2004). Different approaches for the determination of nonlinear aerodynamic ROMs are available in the literature (Lucia et al. 2004, Hall et al. 2000).

In this work it has been chosen to exploit a continuous time recurrent neural network (Mannarino & Mantegazza 2014b) to identify compactly unsteady, nonlinear relations between the structural motion and the aerodynamic loads. After defining the structural dynamics state as $\mathbf{x}_s = [\mathbf{q}_s \ \dot{\mathbf{q}}_s]^{\mathrm{T}}$, the related stable aerodynamic ROM can be appropriately defined with the following set of ordinary differential equations:

$$\begin{cases} \dot{\mathbf{x}}_{\mathrm{a}} & = \mathbf{A}_{\mathrm{ae}}\mathbf{x}_{\mathrm{a}} + \mathbf{B}_{\mathrm{ae}}\mathbf{x}_{\mathrm{s}} + \mathbf{E}_{\mathrm{ae}}\boldsymbol{\phi}\left(\mathbf{x}_{\mathrm{a}}\right) \\ \mathbf{f}_{\mathrm{a}}/q_{\infty} & = \mathbf{C}_{\mathrm{ae}}\mathbf{x}_{\mathrm{a}} + \mathbf{D}_{\mathrm{ae}}\mathbf{x}_{\mathrm{s}} + \mathbf{F}_{\mathrm{ae}}\boldsymbol{\phi}\left(\mathbf{x}_{\mathrm{a}}\right) \end{cases} \tag{19}$$

where $\mathbf{x}_{\mathrm{a}}$ and $\mathbf{x}_{\mathrm{s}}$ are the aerodynamic and structural dynamics state, $\mathbf{A}_{\mathrm{ae}}, \mathbf{B}_{\mathrm{ae}}, \mathbf{C}_{\mathrm{ae}}, \mathbf{D}_{\mathrm{ae}}, \mathbf{E}_{\mathrm{ae}}, \mathbf{F}_{\mathrm{ae}}$ are the ROM parameters, $\mathbf{f}_{\mathrm{a}}$ are the aerodynamic loads and q_{∞} is the flight dynamic pressure. The vectors $\boldsymbol{\phi}\left(\mathbf{x}_{\mathrm{a}}\right)$ are the nonlinear contributions to the ROM dynamics, where each component is an hyperbolic tangent function of the input, i.e. $\phi_i\left(x_{\mathrm{a},i}\right) = \tanh\left(x_{\mathrm{a},i}\right)$. The problem is formulated in the continuous time domain in order to permit variations in the integration time step depending on the analysis under consideration: for example, the time discretization can be modified during the design of a control law where the effect of different sampling times on the closed-loop system may be of interest. Such a variable-time-step feature could also be exploited in the searching of limit cycle oscillation solutions, as reported in (Mannarino & Mantegazza 2014b). As a matter of fact, Eq. 19 represents a nonlinear model in state space form, where the input is the structural dynamics state $\mathbf{x}_{\mathrm{s}}$ while the output is the generalized aerodynamic load $\mathbf{f}_{\mathrm{a}}$. An aerodynamic state is introduced to represent the intrinsic memory the dynamic model: in general it does not have any particular physical meaning. Nonlinear functions like the one employed in this case have already proven their potential in system identification (Haykin 2008).

The training of the reduced order model is addressed in two main stages: the first identifies the linear sub-part, i.e. matrices $\mathbf{A}_{\mathrm{ae}}$, $\mathbf{B}_{\mathrm{ae}}$, $\mathbf{C}_{\mathrm{ae}}$, $\mathbf{D}_{\mathrm{ae}}$, with a classical linear subspace projection technique (Van Overschee & De Moor 1994). The second stage refines the reduced order model response adding the nonlinear terms to the optimization procedure, i.e. matrices $\mathbf{E}_{\mathrm{ae}}$ and $\mathbf{F}_{\mathrm{ae}}$. Because of the intrinsic nonlinearity of the model, a generalized optimization method, i.e. Levenberg-Marquardt (LM) (Marquardt 1963), is employed.

The training signals are generated within the previously described CFD solver. Random-like signals are given in input to all the structural degrees of freedom simultaneously. Amplitude and frequency ranges to be excited are chosen by running a few open loop CFD-based aeroelastic simulations.

4. Flutter Suppression by Immersion and Invariance Control

The basic idea of an Immersion and Invariance (I&I) controller is to achieve a stabilization by immersing the plant dynamics into a stable target system, possibly described by a reduced number of states. Then, by introducing appropriate adaptive

terms in the related controller, it is possible to achieve the invariance of the manifold containing such a target (Astolfi et al. 2008b). The related theory can be found in (Astolfi et al. 2008a), while various applications to aeroelastic systems are reported in (Lee & Singh 2009, 2010a,b, Mannarino & Mantegazza 2014a). The I&I controller presented here is used as a baseline logic to compensate limit cycle oscillations in the ideal system, i.e. with no free-play and actuator dynamics. The computed control effort will then be corrected by the proposed free-play compensation method.

The following strategy is developed by extending to multiple control surfaces the work presented in (Mannarino & Mantegazza 2014a). As will be highlighted, the multi-input formulation of the present controller is different from the single input algorithm detailed in the cited work.

In fact, the designs of the target dynamics, the parameters estimator and the control law are intrinsically coupled, as will be shown in proving the closed-loop stability through Lyapunov function analysis. Therefore, to highlight the peculiar points of the control law development, the design of the I&I controller must be explicitly detailed.

4.1. Design of the target dynamics

The previously mentioned target system $\mathbf{t}$ is here represented by Eq. 20, where $\mathbf{\Lambda}$ is a strictly positive matrix, here assumed as diagonal for sake of simplicity, with positive tunable design parameters $\Lambda_{i,i}$, while $\tilde{\mathbf{y}}$ is the controlled performance, which can be any linear combination of the system state components:

$$\mathbf{t} = \dot{\tilde{\mathbf{y}}} + \mathbf{\Lambda}\tilde{\mathbf{y}} \tag{20}$$

Anticipating that only the displacement at key points of the structure will be taken into account, such a performance can be written as:

$$\tilde{\mathbf{y}} = \mathbf{H}\mathbf{x} = \begin{bmatrix} \mathbf{H}_q & \mathbf{0} \end{bmatrix} \begin{Bmatrix} \mathbf{q} \\ \dot{\mathbf{q}} \end{Bmatrix} = \mathbf{H}_q\mathbf{q} \tag{21}$$

with $\mathbf{H}$ and $\mathbf{H}_q$ defining the appropriate performance output matrix, specified on a case by case basis to define the desired $\tilde{\mathbf{y}}$. Since the performance dynamics must be asymptotically stable over the manifold $\mathbf{t} = 0$, it is sufficient to develop a control law driving $\mathbf{t}$ to the origin. As stated in both Section 1 and 2, this control law is designed for the ideal system without free-play effect, i.e. $\boldsymbol{\beta}_{\text{FP}} = \mathbf{0}$. As will be revealed shortly, this approach permits one to compute directly the control surface deflection required to stabilize the ideal system.

By differentiating Eq. 20, the dynamics of $\mathbf{t}$ is driven by the following equation:

$$\dot{\mathbf{t}} = \ddot{\tilde{\mathbf{y}}} + \mathbf{\Lambda}\dot{\tilde{\mathbf{y}}} \tag{22}$$

where the required $\tilde{\mathbf{y}}$ derivatives can be explicitly defined exploiting Eq. 11:

$$\begin{aligned}\dot{\tilde{\mathbf{y}}} &= \mathbf{HAx} + q_\infty \mathbf{HB}_a\mathbf{f}_a + \mathbf{HB}_d\mathbf{m}_f + \mathbf{HB}_{c_{I\&I}}\boldsymbol{\beta}_c = \mathbf{HAx} = \mathbf{H}_q\dot{\mathbf{q}} \\ \ddot{\tilde{\mathbf{y}}} &= \mathbf{HA}^2\mathbf{x} + q_\infty \mathbf{HAB}_a\mathbf{f}_a + \mathbf{HAB}_d\mathbf{m}_f + \mathbf{HAB}_{c_{I\&I}}\boldsymbol{\beta}_c\end{aligned} \tag{23}$$

The omission of the terms containing $\mathbf{B}_a$, $\mathbf{B}_d$ and $\mathbf{B}_{c_{I\&I}}$ in the first equation above can be trivially inferred by looking at their definitions against that of $\mathbf{H}$. Therefore Eq. 22 becomes:

$$\begin{aligned}\dot{\mathbf{t}} &= \mathbf{HA}^2\mathbf{x} + q_\infty \mathbf{HAB}_a\mathbf{f}_a + \mathbf{HAB}_d\mathbf{m}_f + \mathbf{HAB}_{c_{I\&I}}\boldsymbol{\beta}_c + \boldsymbol{\Lambda}\mathbf{H}_q\dot{\mathbf{q}} \\ &= \boldsymbol{\alpha}\mathbf{x} + q_\infty\boldsymbol{\omega}\mathbf{f}_a + \boldsymbol{\gamma}\mathbf{m}_f + \hat{\mathbf{B}}\boldsymbol{\beta}_c + \boldsymbol{\Lambda}\mathbf{H}_q\dot{\mathbf{q}}\end{aligned} \tag{24}$$

with: $\boldsymbol{\alpha} = \left(\mathbf{HA}^2\right)$, $\boldsymbol{\omega} = (\mathbf{HAB}_a)$, $\boldsymbol{\gamma} = (\mathbf{HAB}_d)$ and $\hat{\mathbf{B}} = \mathbf{HAB}_{c_{I\&I}}$, being unknown constant matrices.
Following the approach proposed in (Lee & Singh 2010b, Tao 2003), the SDU decomposition of $\hat{\mathbf{B}}$ is computed. According to (Tao 2003), $\mathbf{S}$ is a positive definite symmetric matrix, $\mathbf{D}$ a diagonal matrix and $\mathbf{U}$ an upper triangular matrix whose diagonal elements are unitary. Once again, $\mathbf{S}$, $\mathbf{D}$ and $\mathbf{U}$ are unknown matrices, while the elements of $\mathbf{D}$ are assumed to be not null, with their sign being known. In practice, $\mathbf{D}$ can be rewritten as $\mathbf{D} = \eta_{\text{Con}}\hat{\mathbf{D}}$, being η_{Con} the control gain to be tuned during the design. Equation 24 is then rewritten in the following form:

$$\dot{\mathbf{t}} = \boldsymbol{\alpha}\mathbf{x} + q_\infty\boldsymbol{\omega}\mathbf{f}_a + \boldsymbol{\gamma}\mathbf{m}_f + \mathbf{SDU}\boldsymbol{\beta}_c + \boldsymbol{\Lambda}\mathbf{H}_q\dot{\mathbf{q}} \tag{25}$$

Then, after defining the strictly positive matrix $\mathbf{C}_t$, whose elements are design parameters, an asymptotically stable manifold is enforced by adding and subtracting the term $\mathbf{C}_t\mathbf{t}$ to Eq. 25, thus obtaining:

$$\begin{aligned}\dot{\mathbf{t}} &= -\mathbf{C}_t\mathbf{t} + \boldsymbol{\alpha}\mathbf{x} + q_\infty\boldsymbol{\omega}\mathbf{f}_a + \boldsymbol{\gamma}\mathbf{m}_f + \mathbf{SDU}\boldsymbol{\beta}_c + \boldsymbol{\Lambda}\mathbf{H}_q\dot{\mathbf{q}} + \mathbf{C}_t\mathbf{t} \\ &= -\mathbf{C}_t\mathbf{t} + \mathbf{S}\left[\mathbf{DU}\boldsymbol{\beta}_c + \mathbf{S}^{-1}\boldsymbol{\alpha}\mathbf{x} + q_\infty\mathbf{S}^{-1}\boldsymbol{\omega}\mathbf{f}_a + \mathbf{S}^{-1}\boldsymbol{\gamma}\mathbf{m}_f + \mathbf{S}^{-1}\left(\boldsymbol{\Lambda}\mathbf{H}_q\dot{\mathbf{q}} + \mathbf{C}_t\mathbf{t}\right)\right]\end{aligned} \tag{26}$$

Basically $\mathbf{C}_t$ is introduced to guarantee the asymptotic stability of the target dynamics once the control law is designed to compensate all the other terms in the previous equation.
Exploiting the structure of $\mathbf{D}$ and $\mathbf{U}$, the product $\mathbf{DU}\boldsymbol{\beta}_c$ can be decomposed in $\mathbf{DU}\boldsymbol{\beta}_c = \mathbf{D}\boldsymbol{\beta}_c + \hat{\mathbf{U}}\boldsymbol{\beta}_c$, where $\hat{\mathbf{U}}$ is the strict upper triangular part of $\mathbf{U}$, i.e. $\mathbf{U}$ with all the diagonal entries set to zero. Equation 26 can be rewritten in a much more compact form:

$$\dot{\mathbf{t}} = -\mathbf{C}_t\mathbf{t} + \mathbf{S}\left(\mathbf{D}\boldsymbol{\beta}_c + \boldsymbol{\psi}\hat{\boldsymbol{\chi}}\right) \tag{27}$$

Where the matrix $\boldsymbol{\psi}$ is a block diagonal matrix of N_{in} rows, where each block has the following structure:

$$\text{i-th block of } \boldsymbol{\psi} = \left[\mathbf{x}^{\text{T}},\quad q_\infty\mathbf{f}_{\text{a}}^{\text{T}},\quad \mathbf{m}_f^{\text{T}},\quad \left(\boldsymbol{\Lambda}\mathbf{H}_q\dot{\mathbf{q}} + \mathbf{C}_t\mathbf{t}\right)^{\text{T}},\quad \boldsymbol{\beta}_c^{\text{T}}\left(i+1\,:\,N_{\text{in}}\right)\right] \qquad i = 1,\,...,\,N_{\text{in}}-1 \tag{28a}$$

$$\text{Last block of } \boldsymbol{\psi} = \left[\mathbf{x}^{\mathrm{T}}, \quad q_\infty \mathbf{f}_{\mathrm{a}}^{\mathrm{T}}, \quad \mathbf{m}_f^{\mathrm{T}}, \quad \left(\boldsymbol{\Lambda}\mathbf{H}_q\dot{\mathbf{q}} + \mathbf{C}_t\mathbf{t}\right)^{\mathrm{T}} \right] \tag{28b}$$

Where the notation $\mathbf{v}\,(i\,:\,j)$ means that all the elements of $\mathbf{v}$ from position i to position j, are included. The elements of $\mathbf{S}^{-1}\boldsymbol{\alpha}$, $\mathbf{S}^{-1}\boldsymbol{\omega}$, $\mathbf{S}^{-1}\boldsymbol{\gamma}$ and $\mathbf{S}^{-1}$ are arranged accordingly to the structure of $\boldsymbol{\psi}$ in $\hat{\boldsymbol{\chi}}$. In fact, from the stabilization point of view, the order with which the elements of $\hat{\boldsymbol{\chi}}$ are arranged has no importance. At first sight, the main difference of Eq. 27 with the single input controller of Ref. (Mannarino & Mantegazza 2014a, Lee & Singh 2009) is the dependence of $\boldsymbol{\psi}$ on the control effort.

In order to somewhat simplify the I&I design procedure presented in Ref. (Astolfi et al. 2008a), $\mathbf{t} = \mathbf{H}_q\left(\dot{\mathbf{q}} + \boldsymbol{\Lambda}\,\mathbf{q}\right)$, $\boldsymbol{\psi}$ and $\boldsymbol{\beta}_c$ are low pass filtered and attenuated (Seo & Akella 2008, 2009, Lee & Singh 2010a) through with the following equations:

$$\dot{\mathbf{t}}_f = -\mu\mathbf{t}_f + \mathbf{H}_q\left(\dot{\mathbf{q}} + \boldsymbol{\Lambda}\,\mathbf{q}\right) \tag{29a}$$

$$\dot{\boldsymbol{\psi}}_f = -\mu\boldsymbol{\psi}_f + \boldsymbol{\psi} \tag{29b}$$

$$\dot{\boldsymbol{\beta}}_{c,f} = -\mu\boldsymbol{\beta}_{c,f} + \boldsymbol{\beta}_c \tag{29c}$$

where μ is a further positive design parameter. Given that the proposed linear filters are asymptotically stable, it can be shown (Lee & Singh 2010b) that the following ordinary differential equation is satisfied asymptotically:

$$\dot{\mathbf{t}}_f = -\mathbf{C}_t\mathbf{t}_f + \mathbf{S}\left(\mathbf{D}\boldsymbol{\beta}_{c,f} + \boldsymbol{\psi}_f\hat{\boldsymbol{\chi}}\right) \tag{30}$$

4.2. Design of the parameters estimator

Since the parameters vector $\hat{\boldsymbol{\chi}}$ is unknown, I&I approximates it through the aid of shaping terms which will force the stable manifold to be invariant. Within such a view, the off-the-manifold variable $\mathbf{z}$ (Astolfi et al. 2008a) is defined as:

$$\mathbf{z} = \left(\boldsymbol{\chi} + \boldsymbol{\delta}\right) - \hat{\boldsymbol{\chi}} \tag{31}$$

Such a variable is basically a measure of the distance between the estimated parameters $(\boldsymbol{\chi} + \boldsymbol{\delta})$ and the real, unknown ones $\hat{\boldsymbol{\chi}}$, with $\boldsymbol{\delta}(\mathbf{t}_f, \boldsymbol{\psi}_f)$ being a yet to be chosen shaping function, so that, defining a control law of the form $\boldsymbol{\beta}_{c,f} = -\mathbf{D}^{-1}\boldsymbol{\psi}_f\left(\mathbf{z} + \hat{\boldsymbol{\chi}}\right)$, it is possible to cancel the unknown constant parameter vector $\hat{\boldsymbol{\chi}}$ of Eq. 30, which becomes:

$$\dot{\mathbf{t}}_f = -\mathbf{C}_t\mathbf{t}_f - \mathbf{S}\boldsymbol{\psi}_f^{\mathrm{T}}\mathbf{z} \tag{32}$$

As a side note it is remarked that for $\boldsymbol{\delta} = \mathbf{0}$ Eq. 31 recovers the classical formulation of a certainty-equivalent adaptive controller (Slotine & Li 1991). Because of Eq. 31 we have also $\boldsymbol{\beta}_{c,f} = -\mathbf{D}^{-1}\boldsymbol{\psi}_f\left(\boldsymbol{\chi} + \boldsymbol{\delta}\right)$, so that, recalling Eq. 29b and $\dot{\hat{\boldsymbol{\chi}}} = \mathbf{0}, \dot{\boldsymbol{\beta}}_{c,f} = \mu\mathbf{D}^{-1}\boldsymbol{\psi}_f\left(\boldsymbol{\chi} + \boldsymbol{\delta}\right) - \mathbf{D}^{-1}\boldsymbol{\psi}\left(\boldsymbol{\chi} + \boldsymbol{\delta}\right) - \mathbf{D}^{-1}\boldsymbol{\psi}_f\dot{\mathbf{z}}$. Therefore, using Eq. 29c the control law $\boldsymbol{\beta}_c = \mu\boldsymbol{\beta}_{c,f} + \dot{\boldsymbol{\beta}}_{c,f}$

can be written as:

$$\boldsymbol{\beta}_c = -\mathbf{D}^{-1}\boldsymbol{\psi}\left(\boldsymbol{\chi}+\boldsymbol{\delta}\right) - \mathbf{D}^{-1}\boldsymbol{\psi}_f\dot{\mathbf{z}} \tag{33a}$$

or

$$\boldsymbol{\beta}_c = -\mathbf{D}^{-1}\boldsymbol{\psi}\left(\boldsymbol{\chi}+\boldsymbol{\delta}\right) - \mathbf{D}^{-1}\boldsymbol{\psi}_f\left(\dot{\boldsymbol{\chi}}+\dot{\boldsymbol{\delta}}\right) \tag{33b}$$

thus making $\boldsymbol{\beta}_{c,f}$ useless.

In view of ensuring the asymptotic stability of $\mathbf{z}$, let us choose the following shape function: $\boldsymbol{\delta} = \gamma_{\text{Con}}\boldsymbol{\psi}_f^{\text{T}}\mathbf{t}_f$, with γ_{Con} being a positive design parameter. The time derivative of the off-the-manifold variable can now be computed:

$$\dot{\mathbf{z}} = \dot{\boldsymbol{\chi}} + \gamma_{\text{Con}}\left(-\mu\boldsymbol{\psi}_f^{\text{T}} + \boldsymbol{\psi}^{\text{T}}\right)\mathbf{t}_f + \gamma_{\text{Con}}\boldsymbol{\psi}_f^{\text{T}}\left(-\mathbf{C}_t\mathbf{t}_f - \mathbf{S}\boldsymbol{\psi}_f\mathbf{z}\right) \tag{34}$$

so that, imposing the following adaptive definition of $\boldsymbol{\chi}$:

$$\dot{\boldsymbol{\chi}} = -\gamma_{\text{Con}}\left(\boldsymbol{\psi}^{\text{T}} - \mu\boldsymbol{\psi}_f^{\text{T}} - \boldsymbol{\psi}_f^{\text{T}}\mathbf{C}_t\right)\mathbf{t}_f \tag{35}$$

the dynamics of $\mathbf{z}$ is given by:

$$\dot{\mathbf{z}} = -\gamma_{\text{Con}}\boldsymbol{\psi}_f^{\text{T}}\mathbf{S}\boldsymbol{\psi}_f\mathbf{z} \tag{36}$$

At this point, defining $V_z = \frac{1}{2}\mathbf{z}^{\text{T}}\mathbf{z}$ we have:

$$\begin{aligned}\dot{V}_z &= \mathbf{z}^{\text{T}}\dot{\mathbf{z}} = -\gamma_{\text{Con}}\mathbf{z}^{\text{T}}\boldsymbol{\psi}_f^{\text{T}}\mathbf{S}\boldsymbol{\psi}_f\mathbf{z} \\ &\leq -\gamma_{\text{Con}}\lambda_{\mathbf{S},\text{min}}||\boldsymbol{\psi}_f\mathbf{z}||^2\end{aligned} \tag{37}$$

where $\lambda_{\mathbf{S},\text{min}}$ is the smallest eigenvalue of $\mathbf{S}$.. Therefore, $\mathbf{z} = \mathbf{0}$ is an uniformly stable equilibrium point, with $\mathbf{z} \in \mathcal{L}_\infty(0,\infty)$. Moreover, integrating $\dot{V}_z$ the following result is obtained:

$$V_z(\infty) - V_z(0) \leq -\gamma_{\text{Con}}\,\lambda_{\mathbf{S},\text{min}}\int_0^\infty ||\boldsymbol{\psi}_f\mathbf{z}||^2\,dt \tag{38}$$

therefore $||\boldsymbol{\psi}_f\mathbf{z}|| \in \mathcal{L}_2(0,\infty)$. Having obtained the proof of stability for $\mathbf{z}$, we are now able to determine the asymptotic behavior of $\mathbf{t}_f$ defined by Eq. 32. Similarly to the previous calculation, defining $V_t = \frac{1}{2}{\mathbf{t}_f}^{\text{T}}\mathbf{t}_f$ we have:

$$\dot{V}_t = -\mathbf{t}_f^{\text{T}}\mathbf{C}_t\mathbf{t}_f - \mathbf{t}_f^{\text{T}}\mathbf{S}\boldsymbol{\psi}_f\mathbf{z} \leq \lambda_{\mathbf{C}_t,\text{min}}||\mathbf{t}_f||^2 + \lambda_{\mathbf{S},\text{max}}||\mathbf{t}_f||||\boldsymbol{\psi}_f\mathbf{z}|| \tag{39}$$

being $\lambda_{\mathbf{C}_t,\text{min}}$ the smallest element of $\mathbf{C}_t$ and $\lambda_{\mathbf{S},\text{max}}$ the greatest eigenvalue of $\mathbf{S}$. Exploiting Young's inequality, we obtain:

$$\dot{V}_t \leq -\frac{\lambda_{\mathbf{C}_t,\text{min}}}{2}||\mathbf{t}_f||^2 + \frac{\lambda^2_{\mathbf{S},\text{max}}}{2\lambda_{\mathbf{C}_t,\text{min}}}||\boldsymbol{\psi}_f\mathbf{z}||^2 \tag{40}$$

Therefore, since $||\boldsymbol{\psi}_f\mathbf{z}|| \in \mathcal{L}_2\,(0,\infty)$, we have also $||\mathbf{t}_f|| \in \mathcal{L}_2\,(0,\infty)$, thus proving the asymptotic stability of $\mathbf{t}_f$.

4.3. Final control law and proof of stability

At this point, putting together Eqs. 33a and 36, we can explicitly define the control effort $\boldsymbol{\beta}_c$ computed through the I&I logic:

$$\boldsymbol{\beta}_c = -\mathbf{D}^{-1}\boldsymbol{\psi}\boldsymbol{\chi} + \gamma_{\text{Con}}\mathbf{D}^{-1}\left[-\boldsymbol{\psi}_f\boldsymbol{\psi}_f^{\text{T}}\mathbf{t} + \left(\mu\boldsymbol{\psi}_f\boldsymbol{\psi}_f^{\text{T}} - \boldsymbol{\psi}\boldsymbol{\psi}_f^{\text{T}} - \boldsymbol{\psi}_f\boldsymbol{\psi}_f^{\text{T}}\mathbf{C}_t\right)\mathbf{t}_f\right] \tag{41}$$

As the reader can note from Eq. 41, $\boldsymbol{\beta}_c$ seems to be defined in an implicit way, because $\boldsymbol{\psi}$ and $\boldsymbol{\psi}_f$ depend on it. But thanks to the structure of $\boldsymbol{\psi}$, shown in Eq. 28, it should be clear that $\boldsymbol{\beta}_c$ is unique, since it does not depend on $\beta_{c,1}$. In this way, starting from the last line of Eq. 41, the component $\beta_{c,N_{\text{in}}}$ can be evaluated explicitly, so that, all the elements $\beta_{c,i}$ can be backward computed up to $\beta_{c,1}$.

The nonlinear adaptive compensator and its control command are then resumed by Eqs. 29a, 29b, 35 and 41, which are summarized here below for the reader's convenience:

$$\begin{cases} \dot{\mathbf{t}}_f &= -\mu\mathbf{t}_f + \mathbf{H}_q\left(\dot{\mathbf{q}}_o + \boldsymbol{\Lambda}\,\mathbf{q}_o\right) \\ \dot{\boldsymbol{\psi}}_f &= -\mu\boldsymbol{\psi}_f + \boldsymbol{\psi} \\ \dot{\boldsymbol{\chi}} &= -\gamma_{\text{Con}}\left(\boldsymbol{\psi}^{\text{T}} - \mu\boldsymbol{\psi}_f^{\text{T}} - \boldsymbol{\psi}_f^{\text{T}}\mathbf{C}_t\right)\mathbf{t}_f \\ \boldsymbol{\beta}_c &= -\mathbf{D}^{-1}\boldsymbol{\psi}\boldsymbol{\chi} + \gamma_{\text{Con}}\mathbf{D}^{-1}\left[-\boldsymbol{\psi}_f\boldsymbol{\psi}_f^{\text{T}}\mathbf{H}_q\left(\dot{\mathbf{q}}_o + \boldsymbol{\Lambda}\,\mathbf{q}_o\right) + \left(\mu\boldsymbol{\psi}_f\boldsymbol{\psi}_f^{\text{T}} - \boldsymbol{\psi}\boldsymbol{\psi}_f^{\text{T}} - \boldsymbol{\psi}_f\boldsymbol{\psi}_f^{\text{T}}\mathbf{C}_t\right)\mathbf{t}_f\right] \end{cases} \tag{42}$$

with the suffix o indicating that the related quantities are computed using the values that will be provided by a sliding observer, whose implementation details can be found in (Mannarino & Mantegazza 2014a).

To demonstrate the asymptotic stability of the whole control system, we resort to a third Lyapunov function: $W(\mathbf{t}_f, \mathbf{z}) = V_t + V_z$, so that, being:

$$\dot{W} \leq -\frac{\lambda_{\mathbf{C}_t,\text{min}}}{2}||\mathbf{t}_f||^2 - \left(\gamma_{\text{Con}}\lambda_{\mathbf{S},\text{min}} - \frac{\lambda_{\mathbf{S},\text{max}}}{2\lambda_{\mathbf{C}_t,\text{min}}}\right)||\boldsymbol{\psi}_f\mathbf{z}||^2 \tag{43}$$

it can be inferred that the pair $(\mathbf{t}_f, \mathbf{z}) \in \mathcal{L}_\infty(0,\infty)$, if $\gamma_{\text{Con}} \geq 1/\left(2\lambda_{\mathbf{C}_t,\text{min}}\right)\kappa\left(\mathbf{S}\right)$, where $\kappa\left(\mathbf{S}\right)$ is the conditioning number of $\mathbf{S}$, ratio between its maximum and minimum eigenvalues. In practice, the following inequality will be imposed:

$$\gamma_{\text{Con}} \geq \frac{\mathrm{b}_d}{2\lambda_{\mathbf{C}_t,\text{min}}}\kappa\left(\mathbf{S}\right) \tag{44}$$

with b_d being an assigned design bound. Given that the linear filters in Eq. 29 are all asymptotically stable, if $\mathbf{t}_f$ is bounded also $\mathbf{t}$ and, consequently, $\tilde{\mathbf{y}}$ are bounded. Then, the whole state will be bounded and, since W is uniformly continuous, the convergence toward the origin can be proved by using Barbalat's lemma (Slotine & Li 1991).

The meaning of the design parameters $\mathbf{\Lambda}$, $\mathbf{C}_t$, μ, γ_{Con} and η_{Con} should be quite clear: $\mathbf{\Lambda}$ drives the performance to zero when the target manifold is reached, $\mathbf{C}_t$ modulates the convergence toward the stable manifold, μ determines the filtering level of the controller, γ_{Con} is the learning rate of the adaptive law and η_{Con} is the control gain.

5. Free-play and Friction Compensation by Nonlinearity Inversion

A general adaptive approach for controlling systems with actuator free-play nonlinearities and friction is presented here. Such a methodology is employed to neutralize the related nonlinear effects of the actuation control system, so that there is no need to account for such nonlinearities during the controller design. The structural free-play and friction models are assumed to be unknown, and an on-line process will update a set of parameters in order to estimate the free-play semi-width $\boldsymbol{\beta}_{\text{FP}}$, the equivalent control chain stiffness $\mathbf{k}_\beta$ of each control surface and a rough value for the friction amplitude $\hat{m}_f$.

The algorithm here proposed is based on some basic ideas from (Tao 2003), but adopts a different parametrization of the hinge moment, which permits one to identify the unknown parameters separately. Furthermore, differently than (Tao 2003), the problem is formulated in a discrete time framework, thus achieving an immediate digital implementation.

A first version of the present approach was proposed in (Mannarino 2015). Here, the same controller structure is maintained, but the additional feature of the friction torque estimation is included. As will be shown in Section 6.3, such a supplementary estimation further helps the reduction of the closed loop limit cycle oscillations due to the presence of free-play.

The analysis is presented here for a single control surface, because it is assumed that the actuation of a control surface is independent from any other, so it is straightforward to integrate such a control correction for each control surface. The control torque of Eq. 1 can be rewritten in the following form:

$$m_h = m_\beta + m_f + w = k_\beta \left(\Delta\beta + \beta_{\text{FP}}\right) \nu_l + k_\beta \left(\Delta\beta - \beta_{\text{FP}}\right) \nu_r + \hat{m}_f \text{sign}\left(\dot{\beta}\right) + w \tag{45}$$

where $\Delta\beta = z_{\text{act}} - \beta$, w is the assumed measurement noise while:

$$\nu_l = \begin{cases} 1 & \text{for} \quad \Delta\beta < -\beta_{\text{FP}} \\ 0 & \text{otherwise} \end{cases} \tag{46a}$$

and

$$\nu_r = \begin{cases} 1 & \text{for} \quad \Delta\beta > \beta_{\text{FP}} \\ 0 & \text{otherwise} \end{cases} \tag{46b}$$

Since k_β, β_{FP} and $\hat{m}_f$ in Eq. 45 are assumed to be unknown, they can be collected in the unknown vector $\boldsymbol{\theta} = \{\theta_1\ \theta_2\ \theta_3\} = \{k_\beta\ \beta_{\text{FP}}\ \hat{m}_f\}$. Eq. 45 can then be rewritten as:

$$m_h = \theta_1 \left(\Delta\beta + \theta_2\right) \nu_l + \theta_1 \left(\Delta\beta - \theta_2\right) \nu_r + \theta_3 \text{sign}\left(\dot{\beta}\right) + w \tag{47}$$

where of course the variable β_{FP} is substituted by θ_2 in the definition of ν_l and ν_r in Eqs. 46.

The vector $\boldsymbol{\theta}$ is updated at each sampling instant by means of a simple gradient descent algorithm (Haykin 2008):

$$\boldsymbol{\theta}_{n+1} = \boldsymbol{\theta}_n - \eta^{\text{GD}} \frac{\partial e_n}{\partial \boldsymbol{\theta}_n} \tag{48}$$

where η^{GD} is the classical learning rate, while e_n is the instantaneous output error, defined as:

$$\begin{aligned} e_n &= m_{h,n}^{\text{meas}} - m_{h,n} \\ &= m_{h,n}^{\text{meas}} - \theta_{1,n} \left(\Delta\beta_n + \theta_{2,n}\right) \nu_{l,n} - \theta_{1,n} \left(\Delta\beta - \theta_{2,n}\right) \nu_{r,n} - \theta_{3,n} \text{sign}\left(\dot{\beta}_n\right) + w \end{aligned} \tag{49}$$

$m_{h,n}^{\text{meas}}$ is the torque output of Eq. 6. Since the derivative $\frac{\partial e_n}{\partial \boldsymbol{\theta}_n}$ is required by Eq. 48, it is provided here by its explicit definition, which can be directly obtained from Eq. 49:

$$\begin{aligned} \frac{\partial e_n}{\partial \theta_{1,n}} &= -\left(\Delta\beta_n + \theta_{2,n}\right) \nu_{l,n} - \left(\Delta\beta - \theta_{2,n}\right) \nu_{r,n} = -\Delta\beta_n \left(\nu_{l,n} + \nu_{r,n}\right) + \theta_{2,n} \left(\nu_{r,n} - \nu_{l,n}\right) \\ \frac{\partial e_n}{\partial \theta_{2,n}} &= -\theta_{1,n}\nu_{l,n} + \theta_{1,n}\nu_{r,n} = \theta_{1,n} \left(\nu_{r,n} - \nu_{l,n}\right) \\ \frac{\partial e_n}{\partial \theta_{3,n}} &= -\text{sign}\left(\dot{\beta}_n\right) \end{aligned} \tag{50}$$

Following the approach proposed in (Tao 2003), the desired hinge moment can be computed as:

$$m_{h,n}^{\text{des}} = \theta_{1,n} \Delta\beta_n^{\text{ideal}} \tag{51}$$

where $\Delta\beta_n^{\text{ideal}}$ is the ideal aileron dynamic response, i.e. $\beta_{\text{FP}} = 0$, resulting in $\Delta\beta_n^{\text{ideal}} = \beta_{\text{ext},n} + \beta_{c,n}^{\text{I\&I}} - \beta_n$, where $\beta_{c,n}^{\text{I\&I}}$ is the outcome of the Immersion and Invariance control logic defined by Eq. 41. Having a law available which minimizes the

output error of Eq. 49, the free-play nonlinearity can now be inverted to obtain the desired aileron motion:

$$\Delta\beta_n^{\text{des}} = \begin{cases} \dfrac{m_{\beta,n}^{\text{des}} - \theta_{1,n}\theta_{2,n} - \theta_{3,n}\text{sign}\left(\dot{\beta}\right)}{\theta_{1,n}} & \text{for} \quad m_{\beta,n}^{\text{des}} < 0 \\ 0 & \text{for} \quad m_{\beta,n}^{\text{des}} = 0 \\ \dfrac{m_{\beta,n}^{\text{des}} + \theta_{1,n}\theta_{2,n} - \theta_{3,n}\text{sign}\left(\dot{\beta}\right)}{\theta_{1,n}} & \text{for} \quad m_{\beta,n}^{\text{des}} > 0 \end{cases} \tag{52}$$

with the new control input computed as:

$$\beta_{c,n} = \Delta\beta_n^{\text{des}} - \beta_{\text{ext},n} + \beta_n \tag{53}$$

So making explicit the input to Eq. 17. Such a control law should be able to "jump" across the free-play range, neutralizing its nonlinear effect. Within such a framework, the proposed compensation technique can be interpreted as a control augmentation algorithm which can be easily exported to any control logic.

Summarizing, the whole compensation strategy can be described in two main points:

- An Immersion and Invariance-based control law is designed to stabilize the ideal system, i.e. $\beta_{\text{FP}} = 0$, as explained in Section 4,
- A correction to the control input, required to neutralize the free-play effect, is calculated by means of the algorithm presented in this Section.

As it is clear, the measurements required to implement what was just presented are usually available within any actual control surface servo-system employed in aeronautical applications. Thus it is worth stressing that by encompassing a reasonable friction, the identified hinge moment needs not to be close to the true value associated with the inertia and aerodynamic control loads. Therefore, by way of example, in an hydraulic servo it would suffice to know just the net pressure acting on the ram piston and the rotation of the control surface, which would be used to evaluate the related inertia forces through finite differences. Moreover, even if the identified friction load is somewhat approximate, it is important to take into account that its value must provide just a support to a better inversion of the free-play. Furthermore the considered application will show that the adopted identification approach is robust enough to allow embedding the hinge friction within the unstructured noise, w, without a substantial detrimental effect. In fact it has been verified that even a priori precise estimates of the free-play and stiffness, such as those measurable on the ground on the actual flying aircraft, would provide a substantial compensation of a residual, free-play induced limit cycle. Despite that, since it allows to maintain good performance against long term usage, eventual wear, changing environmental conditions and loads, the most effective on-line identification should always be preferred.

6. A Sample Application

The previously presented technique is applied to a plunging and pitching NACA 0012 airfoil, flying at $M_\infty = 0.8$ in air. The airfoil is equipped with fully unbalanced leading and trailing edge controls, whose hinges are placed at 15% and 80% of the chord respectively. A schematic representation of the system is given in Fig. 2a, while the related structural data can be found in the Appendix. After a convergence analysis based on static aerodynamic data of a simply pitching airfoil, a C-type topology mesh is discretized with 32000 elements, increasing the cells density near the control surfaces hinges, in order to track the local surface motion with an higher accuracy, as shown in Fig. 2b.

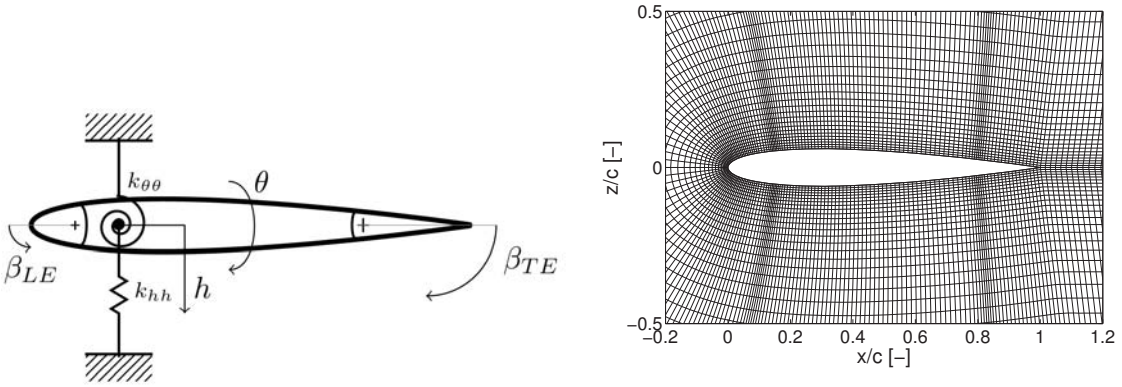

(a) Mechanical model.

(b) Computational mesh - close up.

Fig. 2. Four degrees of freedom typical section model.

6.1. Reduced order modeling and simulations

Once the full order system is defined, we can extract reduced order models from it. The input-output pair used in the training stage is shown in Fig. 3. From a linearized analysis of the high fidelity model, the flutter eigenmode and frequency are available. We use this information to compute the training signal: all the degrees of freedom are excited simultaneously by a random-like motion. The frequency content of the signal is evaluated through its Fast Fourier Transform (FFT), so it can be designed to present a peak of its FFT around the flutter frequency, which is $f_{\text{bif}} = 9.3$ Hz. The flutter eigenmode provides a rough estimate of the motion amplitudes at the flutter point. This information is used to assign the root mean square value of the training signal. Such a training signal is generated by feeding the structural motion input depicted in Fig. 3a to the CFD solver, which computes the load history of Fig. 3b. The time required to compute this input-output relation is about 12 hours on 4 CPU units. The simulation is run with a physical time step $\Delta t_{\text{CFD}} = 10^{-3}$ seconds, using a 5th order accurate Runge-Kutta scheme, setting the CFL number to a value of 3. The convergence between time steps is accelerated by multigrid and dual time stepping methods. A series of ROMs are then computed considering an increasing number of aerodynamic states N_a, from 5 to 12. The average training time required to compute the matrices entries of the ROM is about 6 hours. Such a convergence analysis is carried out assuming as target value the bifurcation velocity

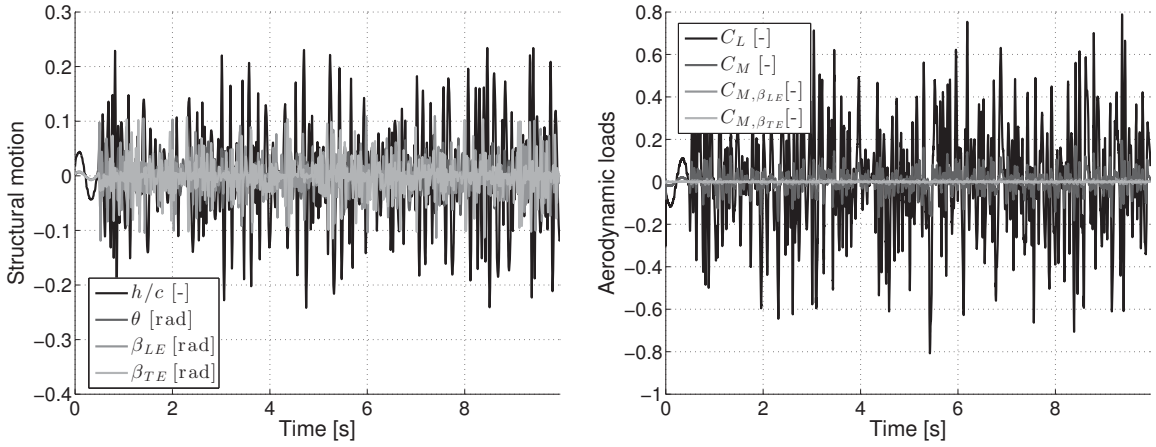

(a) Input: structural motion.

(b) Output: aerodynamic loads.

Fig. 3. Training signal.

of the system, usually available from linearized analyses, resulting in $V_{\infty,\text{bif}} = 160.68$ m/s. A comparison between CFD and ROM based results is provided in Fig. 4. It is evident that increasing the number of states leads to a better matching between CFD and ROM-based results. However, it is interesting to note how the results with $N_a = 6$ present the same trend of the CFD, slightly shifted to the left. By contrast, the results with $N_a = 12$, although showing a smaller overall error, exhibit a local trend slope quite different from the reference data. From a design point of view, the results obtained with $N_a = 6$ would be preferred, because, by exhibiting a lower bifurcation speed, they are conservative and closer to the shape of the reference curve. Nevertheless, in the control law design the model with $N_a = 12$ will be employed, showing that the proposed strategy is robust enough to deal with this kind of modeling error. Once trained, the ROM permits us to

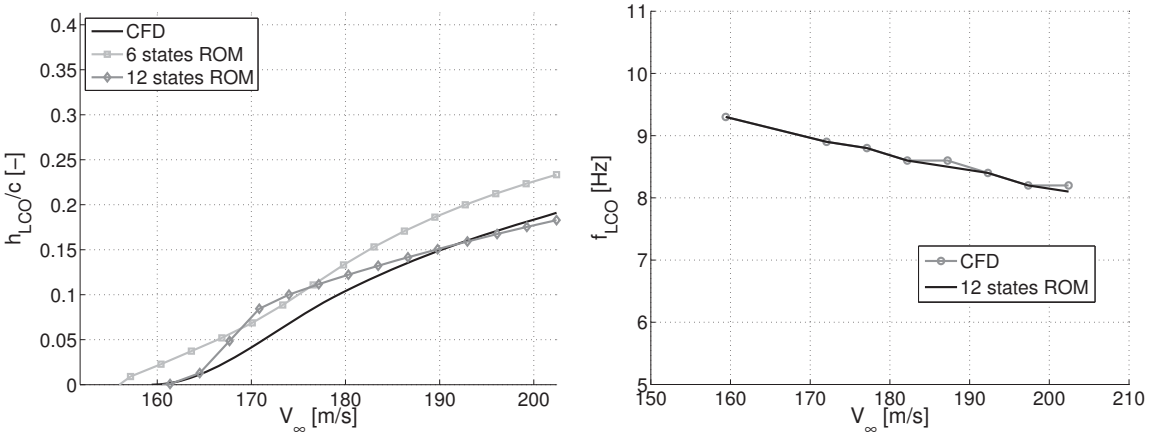

(a) Plunge LCO amplitude versus flight speed.

(b) LCO frequency versus flight speed.

Fig. 4. Sample of LCO amplitude and frequency trends.

carry out design simulations at a faster pace than with CFD based aerodynamics. In fact, a CFD model would take an hour to calculate what the ROM provides in 2 seconds, with no significant loss of accuracy.

At this point, structural free-play and a Stribeck modeled friction are introduced in the control surface actuation systems, and the effects of these nonlinearities on the LCO response are evaluated. The free-play semi-width considered in the following analyses is $\beta_{\text{FP}} = 0.15$ deg for both the leading and trailing edge control surfaces. These values should be considered rather high, since aircraft certification standards require very tight control surface free-play limits (a fraction of a degree) (Kholodar 2014). The related results are shown in Fig. 5. The system is excited with different pulses introduced by the trailing edge control surfaces. It is clear that as the amplitude of the pulse is varied, the system behavior changes radically: if the pulse is sufficiently strong and the flight speed is sufficiently high, then aerodynamically induced LCOs would be activated. Instead, at lower flight speeds with weaker perturbations, self-excited oscillations are governed by the free-play effect, resulting in much smaller amplitudes. It is thus clear that 'hard' nonlinearities, such as free-play and friction, lead to a stronger dependence of the system response on the type of perturbation used. The results are also compared with the ideal trends, i.e. without free-play. The corresponding switching points are further moved ahead as the free-play width is increased: as it will be shown later on, at the same flight speed it is possible to experience either a large amplitude, aerodynamically driven LCO when the free-play width is small enough, or a small amplitude, free-play driven LCO when the mentioned width is increased. A further comparison is also provided through a slowdown test: the system is perturbed and left free to reach a large amplitude LCO, then the velocity is gradually reduced and the oscillation amplitude is tracked. As witnessed by the black dash-dotted curve in Fig. 5, an hysteretic cycle is present in the response, whereas large oscillations are experienced even at low speeds. With respect to the work presented in (Mannarino & Mantegazza 2014a), the presence of the free-play in the control surface actuation system leads to a bistable behavior which makes the analysis of this problem interesting. Therefore the aeroelastic system is able to produce both aerodynamically or free-play driven limit cycle oscillations, depending on the initial condition and on the type of input used to excite the system. This behavior requires a deeper investigation and it is currently under study by the authors.

6.2. Control system settings

After several open loop simulations, the sensors parameters are set to $\xi = 1$ and $\omega_{\text{acc}}, \omega_{\text{sens}} = 220$ rad/s. Such values are mostly dictated by the assumption of a second order anti-aliasing filter for the digital implementation, whose bandwidth is significantly below the one of the related sensor.

It is recalled that the presented results are related to the real system, i.e. the one including the servo dynamics, while the control law is designed without considering it. It must however be stressed that, even if the actuator dynamics does not appear in the I&I control law formulation, its effect is fully taken into account, i.e. see Eq. 17, during the controller tuning, because, as proved in (Mannarino & Mantegazza 2014a), a basic modeling of the actuation system is required to achieve a good level of robustness of the adaptive law against variations of the actuator bandwidth. Thus, the controller will be tuned on the system including such additional elements, verifying in this way also the strength of the proposed method against unmodeled dynamics. In what follows, the nominal value of the actuators parameters is set to $\xi_{\text{act}} = 0.65$ and $\omega_{\text{act}} = 107$

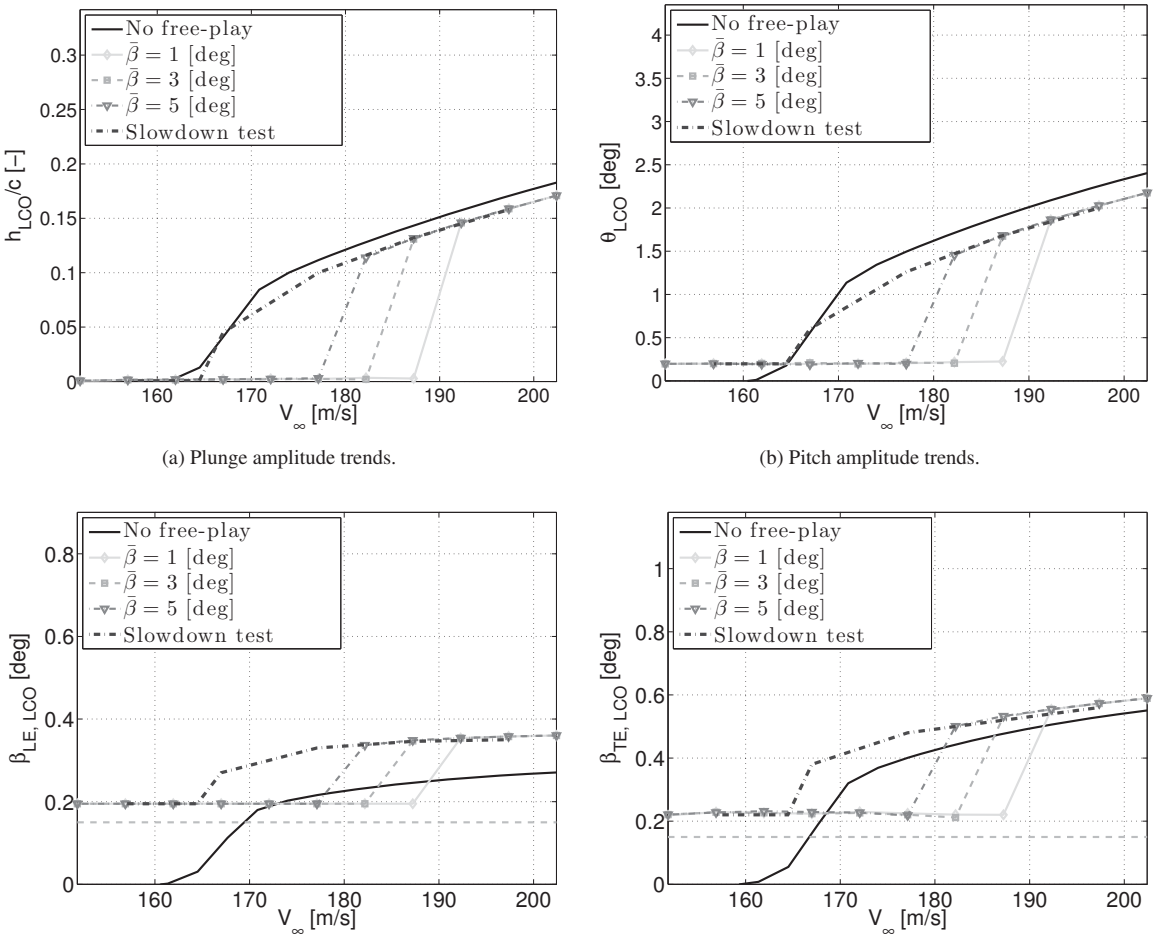

(a) Plunge amplitude trends.

(b) Pitch amplitude trends.

(c) Leading edge oscillation amplitude trends.

(d) Trailing edge oscillation amplitude trends.

Fig. 5. Comparison of the LCO trends with and without free-play.

rad/s. The actuators saturate in position at 15 deg and in rate at 45 deg/s. As it will be seen in the following results, such a bandwidth is not sufficient to guarantee a complete removal of the residual LCOs from the closed loop response. Even if the assumed bandwidth is a somewhat conservative specification, being clearly more demanding than what is strictly needed to suppress a simple flutter (Mannarino & Mantegazza 2014a), a higher performance is required when dealing with free-plays, because they require a sort of fast 'jump' between the limits of the deadzone band, thus requiring a very quick actuator response to follow the computed control effort. In fact, it is anticipated that sensitivity analyses will assess the influence of the actuator bandwidth on the compensation performance of the controller, showing, as expected, that the faster an actuator is, the better results can be achieved.

The controller design could have been carried out either interactively or through a numerical optimization which, because of the relatively low system order and smooth dependence on a small number of parameters, could have been based on an efficient gradient free optimizer, e.g. (Rios & Sahinidis 2013, Powell 2006). The former option has been preferred. In fact, as verified in (Mannarino & Mantegazza 2014a), such an approach requires no further coding and can be easily guided

by following a simple heuristic procedure, based on the previously hinted physical understanding of the design parameters. The filter parameter μ is typically chosen in relation to the maximum frequency of the open loop response, estimated by Fourier transforming a few time histories. Then, after verifying that a tentative $\mathbf{C}_t = \text{diag}\,(1)$ can be a suitable choice, γ_{Con} is computed accordingly to Eq. 44, followed by a few analyses carried out by maintaining $\mathbf{\Lambda} = \text{diag}\,(1)$, while determining appropriately the values of $\mathbf{C}_t$, γ_{Con} and η_{Con} leading to a reasonable maximum control effort, eventually increasing the value of diagonal elements of $\mathbf{\Lambda}$ until a desired settling time is achieved. A value of $\text{b}_d = 2$ proved sufficient to achieve an adequate level of robustness.

To assure the system adaptivity and stability over a wide range of operating conditions, the controller parameters are tuned over various flight speeds, combined with different type of simulations, such as the response to large initial conditions, to input pulses, and evaluating the controller adaption speed when its compensator is switched off-on during a simulation, eventually considering various free-play widths and friction models.

All the tuned designs and verifications have been determined by using an explicit Runge-Kutta integrator with adaptive step control, providing a precision adequate to allow an exact matching of the so called 'hard' nonlinearities, i.e. free-play, friction and saturations in the actuators output, which are present in all the simulations. Moreover a realistic digital implementation of the proposed controller has been taken into account. Through some preliminary continuous designs, it has been possible to verify that the sampled behavior of the continuous compensator can be adequately matched at a frequency of 180 Hz, with the related discretization based on a fix step Heun integration scheme. Moreover it has been preferred to envisage a somewhat more realistic implementation, where the free-play cancellation is embedded within the control surface servos, which are mostly self contained black boxes with their own independently digitalized realization. Thus, in order to provide a negligible phase shift against deflection commands, provided at a different (in general lower) rate, the control servos are mostly run at a higher sampling rate, which will be here assumed to be 400 Hz. To simulate correctly such a digitalization there is the need to care for the processing delay (input-calculation-output), associated with the chosen data acquisition system and control computer, in this case set to 1.7 ms. As described in Sections 1 and 5, an equivalent average Coloumb like approximation of structural friction is identified by the control law. Instead, the actual plant is characterized by a more realistic Stribeck model (Ferretti et al. 2003), whose parameters are tuned to give a maximum friction torque comparable to the one computed by the simpler model.

A substantial set of simulations has been carried out for various ROM and finely discretized aerodynamic models, measurement noise, disturbances and large changes of the free-play parameters.

6.3. Discussion of the main results

After being validated in the previous section, the reduced order aeroservoelastic model is here employed in the design of the control law. The total number of states of the compacted model is 32: 8 structural, 12 aerodynamic, 8 for the sensors

and 4 for the actuators. The total number of states required to describe the high fidelity, CFD-based system is equal to 128020, showing once again that a design carried out on such a model would have been impractical.

The following results are so organized: first it will be shown that even an I&I controller designed on the ideal system is able to suppress the main limit cycle behavior of the system, yet does not remove the residual LCO due to the control surface free-play. Then the results related to the design model with active free-play compensation system will be presented. Finally, a few verification tests where the aerodynamic sub-system is simulated by a full CFD solver will be discussed.

To achieve good adaptive performances against pulse perturbations applied through the trailing edge control surface, different flight speeds, up to 25% higher than $V_{\infty,\text{bif}}$, are taken into account to tune the controller parameters. The target performances of Eq. 21 are the plunge and pitch of the typical section. Two accelerometers are placed at the 20% and at the 70% of the chord respectively, maximizing in this way the signal to noise ratio and thus making the reconstruction of the structural state easier.

Carrying out the design on the ideal system, i.e. $\beta_{\text{FP}} = 0$, with the interactive procedure previously described, the control parameters of Table 1 are obtained:

γ_{Obs}	$\mathbf{\Lambda}$	$\mathbf{C}_t$	μ	γ_{Con}	η_{Con}
0.5	$\text{diag}(150)$	$\text{diag}(50)$	750	0.1	100

Table 1: Controller parameters.

Being $\kappa(\mathbf{S}) = 1$, the inequality of Eq. 44 is satisfied, guaranteeing the stability and robustness of the controller. A comparison of open and closed loop responses for the ideal system with the parameters of Table 1 is shown in Figure 6. All the coefficients are tuned considering responses to input pulses of the trailing edge control surface, over flight speeds ranging from $V_{\infty,\text{bif}}$ to 1.15 $V_{\infty,\text{bif}}$. As can be seen, the system is efficiently stabilized by the designed controller. At this point free-play and friction are introduced into the system model. Computing a few open loop responses due to input pulses, the amplitude of friction torque on both hinges has been set to 20% of the actual torque transmitted by the actuator. Introducing the free-play nonlinearity in the control surface actuation, the closed loop response is partially deteriorated, as witnessed by Figure 7. The designed control law is still able to reduce the amplitude of the limit cycle oscillations, but residual vibrations due to the presence of the control surface free-play show up, making the closed loop response unacceptable. The free-play compensation is then introduced, with the aim of further reducing the residual LCO in the closed loop response. The only parameter that should be set in this case is the learning rate η^{GD} of Eq. 48. As a rule of thumb, the designer should start with a fairly low value, e.g. 0.01, then increase it until a sufficiently fast convergence rate of the free-play parameters is obtained. Following this simple procedure, in the present case the best results are obtained with $\eta^{\text{GD}} = 1.25$. From authors' experience, low values of η^{GD} lead to stable but slowly converging results, while for values of η^{GD} too high, e.g. 2, the training process of Eq. 48 can become unstable. The initial value for the unknown free-play parameters of Eq. 47 has been chosen through some guided trials: their value is not known, but their rough estimate can

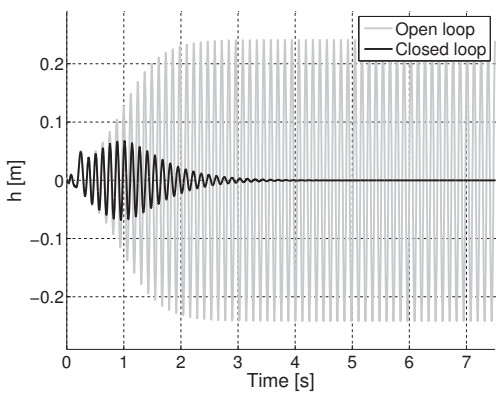

(a) Plunge response.

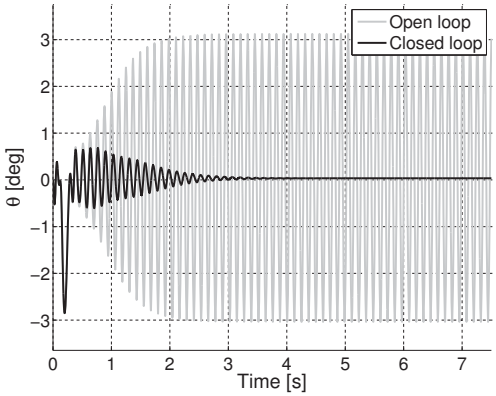

(b) Pitch response.

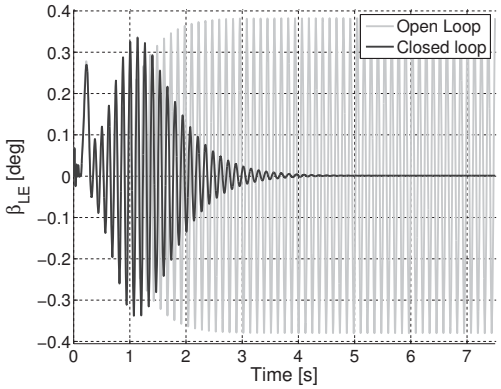

(c) Leading edge deflection.

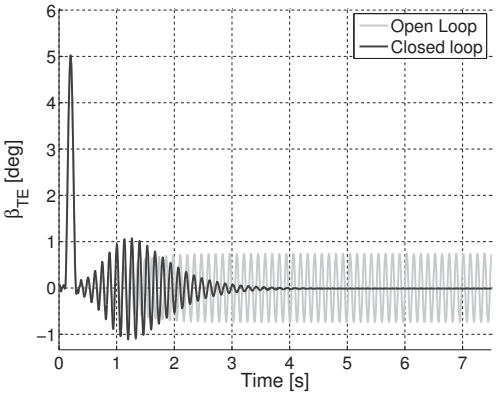

(d) Trailing edge deflection.

Fig. 6. Ideal system response to an input pulse, $V_\infty = 188$ m/s.

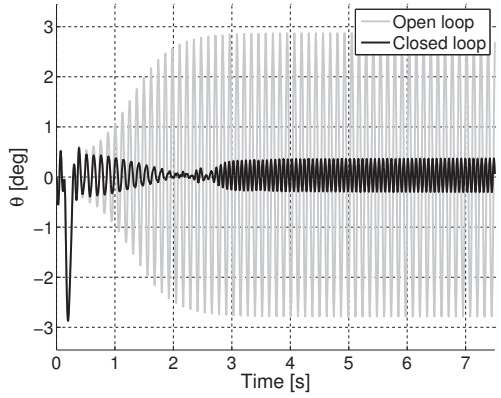

(a) Pitch response.

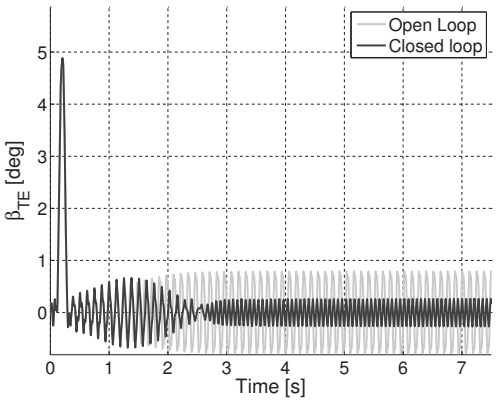

(b) Trailing edge deflection.

Fig. 7. System response to an input pulse, free-play present but not compensated, $V_\infty = 188$ m/s.

be easily assumed. With this idea in mind, we set randomly the initial value for the free-play parameters, oscillating from -50% to $+50\%$ of their true value. The closed loop response with the free-play compensator maintained active during the simulation is shown in Figure 8: the free-play effect is reduced to a remarkably low level, with almost no residual oscillations. The convergence history of the unknown free-play parameters can be tracked, their history being shown in

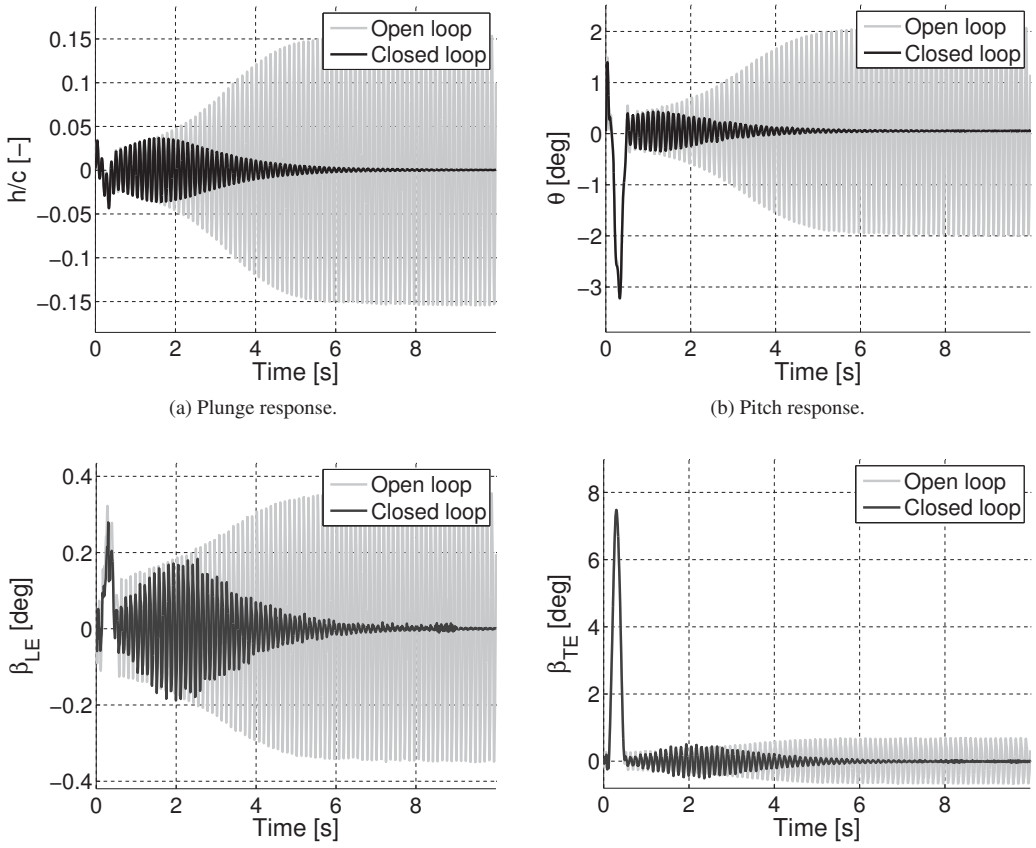

(a) Plunge response.

(b) Pitch response.

(c) Leading edge deflection.

(d) Trailing edge deflection.

Fig. 8. System response to an input pulse with compensated free-play, $V_\infty = 188$ m/s.

Figure 9. A fairly small final error has been obtained, and this can be considered a very good result for two main reasons. First: for each control surface, we are trying to estimate three different parameters starting from only a single error measure, which combines them. Second: the system is not "persistently excited" (Tao 2003, Slotine & Li 1991) and this may have led to inaccurate identification results. For better appreciating the compensation effect of the proposed control law a phase space plot of the control surfaces deflection is shown in Figure 10. As a verification of the results obtained with the design model, the compensator is tested on a system excited by aerodynamic loads computed directly by using a fine Euler-based CFD solution. In this test the system is left free to reach an LCO condition. Then the control law is activated, eventually driving the response to zero. This kind of test can be useful for assessing possible dynamics that have not been captured by the reduced order model. Furthermore, switching on the controller only after the LCO has been reached permits one to evaluate its robustness in a case where the system nonlinearities are completely developed. To make the test even more challenging, a random disturbance with a root mean square of 0.1 deg is directly applied to the trailing edge control surface and the free-play of both control surfaces is set to $\beta_{\text{FP}} = 0.2$ deg. The response obtained is shown in Figure 11, where the control law is activated after four seconds of simulation. It should be noted that the control law is still able to stabilize the response, even if a small residual LCO is still present, as witnessed by Figure 12. A further verification is carried out

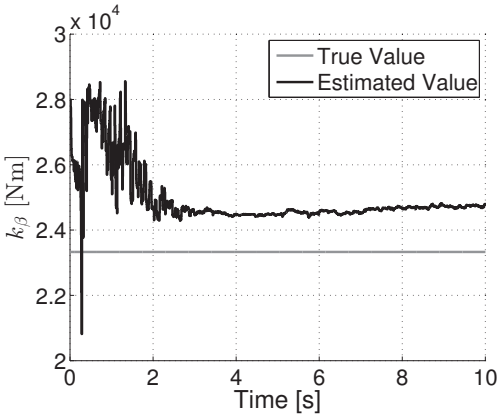

(a) Convergence of the leading edge command stiffness.

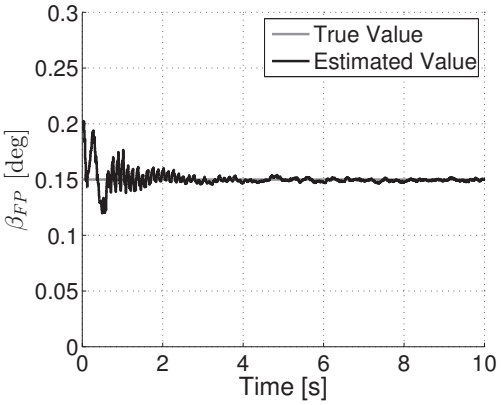

(b) Convergence of the trailing edge free-play width.

Fig. 9. Convergence history for the unknown parameters of the free-play model.

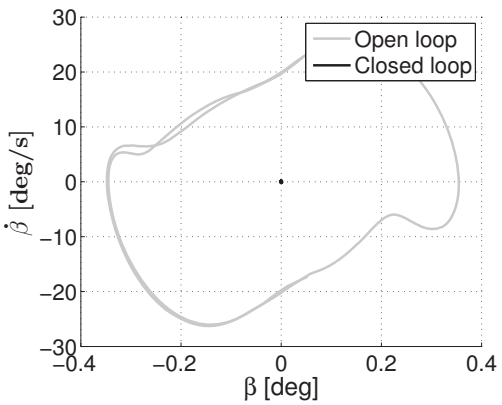

(a) Comparison of leading edge LCOs.

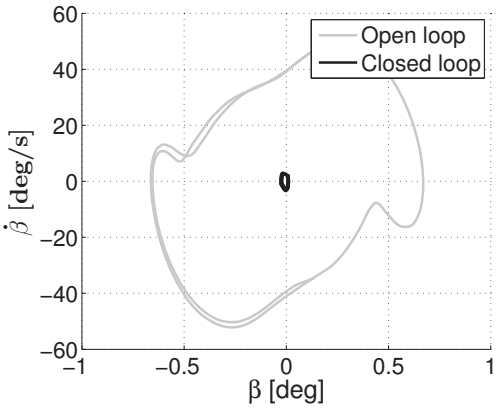

(b) Comparison of trailing edge LCOs.

Fig. 10. Phase space plots of the control surfaces deflection.

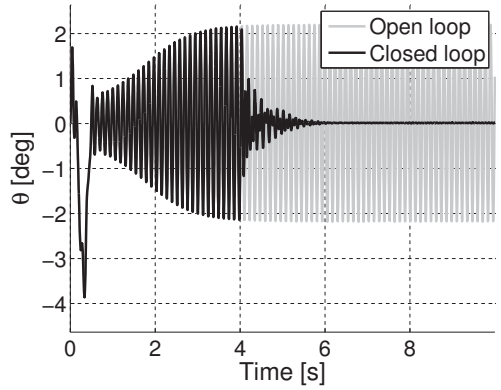

(a) Pitch response.

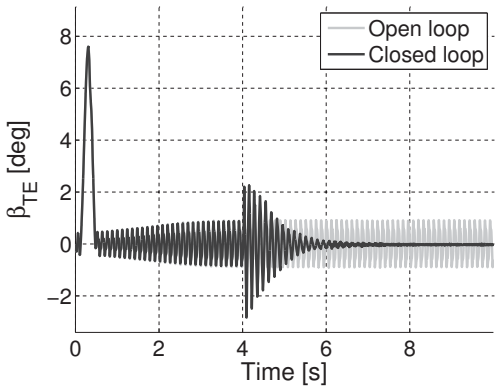

(b) Related control effort.

Fig. 11. Verification response to off/on control, $V_\infty = 205$ m/s.

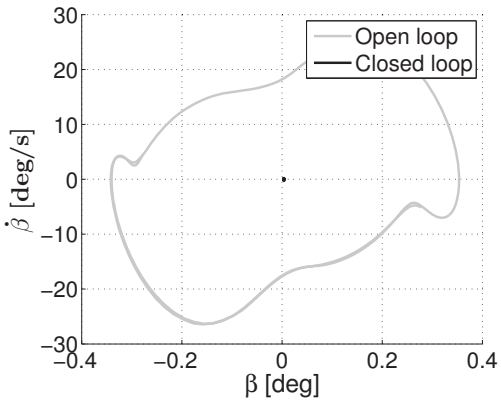

(a) Comparison of leading edge LCOs.

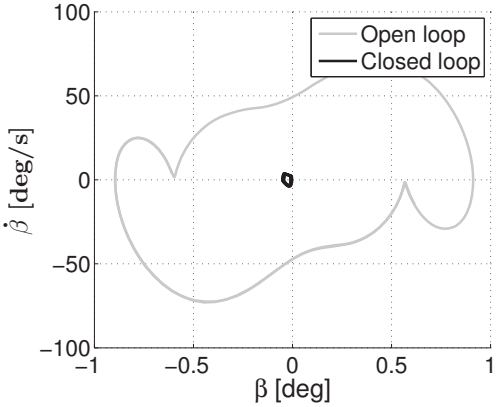

(b) Comparison of trailing edge LCOs.

Fig. 12. Phase space plots of the control surfaces deflection, $V_\infty = 205$ m/s.

considering larger values of the free-play width, now set to $\beta_{\text{FP}} = 0.25$ deg for each control surface and a 30% reduction of their stiffness. As evidenced by Figure 13, now the open loop LCO is driven by the free-play nonlinearity, leading to much smaller motion amplitudes. It is therefore interesting to observe how the designed controller is also able to adapt and stabilize the system in such very different circumstances. Furthermore, as shown in Figures 13c and 13d, a sizeable free-play reduction can be otained by discarding the friction torque from the identification procedure, even if the estimation of its average effect helps to further reduce the residual LCOs in closed loop. The free-play induced LCO is reduced to a fairly low amplitude even if the free-play width is relatively large in this case, proving once again the effectiveness of the proposed compensator. In addition, the proposed controller is quite insensitive even with a not so precise modeling of the friction torque, nevertheless identifying a comparable averaged value of its amplitude in any performed simulation, thus helping in the compensation of the nonlinearities present in the actuation system. The robustness of the compensation system is now verified in face of variations of the actuators bandwidth, while the flight speed is maintained constant at $V_\infty = 195$ m/s. The results are shown in Figure 14, where the bandwidth is varied from 32 to 8 Hz. As expected, a reduction of the bandwidth results in a reduction of the control system effectiveness. For frequencies lower than 15 Hz,

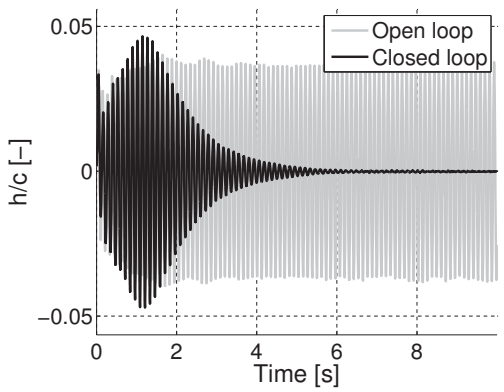

(a) Plunge response.

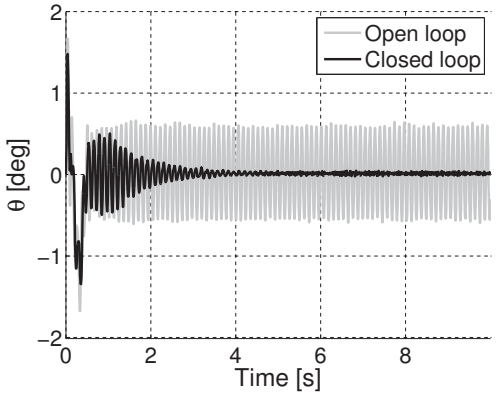

(b) Pitch response.

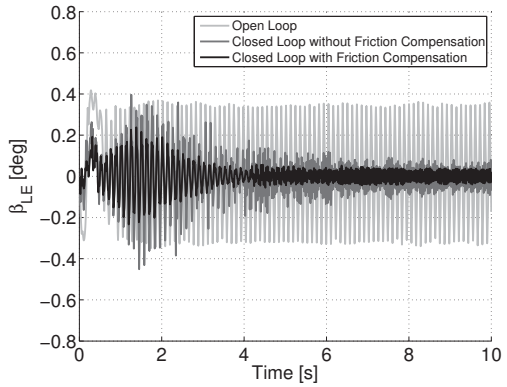

(c) Leading edge deflection.

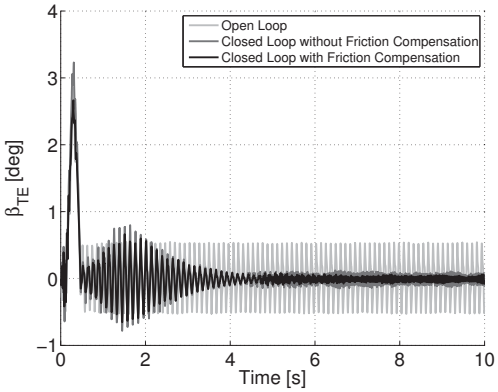

(d) Trailing edge deflection.

Fig. 13. Verification response with large free-play width, $V_\infty = 205$ m/s.

usually sufficient in classical flutter stabilizations (Waszak 1997, Mannarino & Mantegazza 2014a), the residual LCOs in closed loop are comparable to the one experienced in open loop. It is therefore clear that the suppression of control surfaces free-play requires higher performance servos.

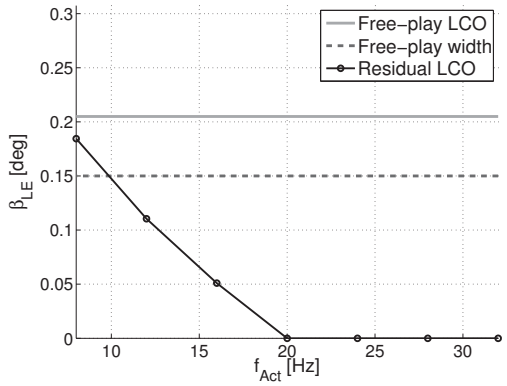

(a) Sensitivity analysis on the leading edge control surface actuator.

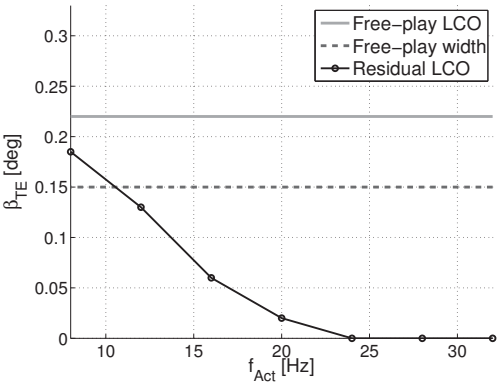

(b) Sensitivity analysis on the trailing edge control surface actuator.

Fig. 14. Sensitivity of the LCO compensation effectiveness versus the actuators bandwidth.

Finally, the ability of the controller to widen the flutter-free flight range is investigated. Several simulations with increasing

velocities are carried out. As seen in Figure 15, the flutter point is moved forward to 57% of its initial value. This result is obtained by considering off/on simulations, which have proven to be the most challenging tests for the presented controller. Now, considering pulse perturbations with different amplitudes, indicated by $\bar{\beta}$ in the figure, the flutter-free envelope is widened even more, moving back to the off/on results as the pulse amplitude is increased. It is also interesting to see how the flutter trends change with the presence of the controller: while the open loop system shows a range where the LCO amplitudes gradually increase with the flight speed, the closed loop envelope presents a sort of 'linear' instability point, beyond which the system produces very large oscillations, as for the unstable response of a linear system. Analyzing again Figure 15, it is clear that going towards the bifurcation point the basin of attraction of the stable solution is shrinking, so LCOs are obtained for smaller and smaller perturbations. Again, this fact should be studied more in depth, but is beyond the scope of the present paper.

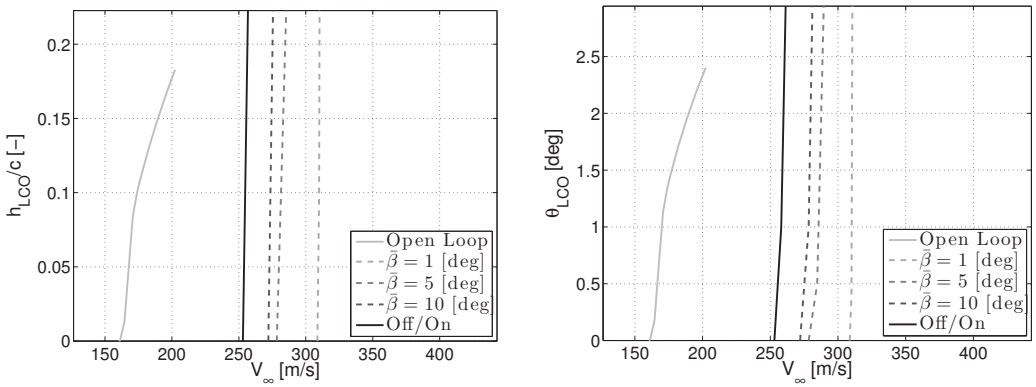

(a) New plunge flutter envelope.

(b) New pitch flutter envelope.

Fig. 15. Closed loop flutter envelopes, each one obtained considering different perturbations.

7. Conclusions

This work has presented an adaptive control strategy for compensating the effect of free-play and friction in a nonlinear servo actuator for active flutter suppression. The approach uses a controller designed in two stages, where the first one is devoted to the stabilization of the flutter at flight speeds beyond the stability boundary, while a second controller compensates residual limit cycle oscillations due to the presence of free-play and friction in the control surface mechanism. The resulting control logic is a combination of an Immersion and Invariance and a nonlinearity inversion approach. Differently from the approaches previously found in the literature, such an inversion method is formulated here in a way that enables an independent identification of the free-play parameters and an averaged friction amplitude. Even though only numerical simulations are considered in this work, the presented results can be considered encouraging and could constitute a basis for a realistic implementation of the algorithms here described. Because of the small number of design parameters, the adopted interactive design procedure, based on well-reasoned and physically understood simulations, it has been verified to be an adequate design method. In fact, the resulting adaptive controller provided fairly robust stabilization properties against

differing flow conditions, disturbances, model orders and parameter variations. As a further development of the present results, one could focus on more complex and realistic applications, e.g., (1) deformable, free-flying aircraft, (2) extending the proposed methodology to the context of load alleviation, (3) integrating true design specifications related to stability and response performances, while (4) trying also to make the tuning process automatic through the use of optimization techniques.

A. Model Data

$$\mathbf{M}_s = \begin{bmatrix} m & S_{h\theta} & S_{h\beta_{\text{LE}}} & S_{h\beta_{\text{TE}}} \\ & J_\theta & 0 & 0 \\ & & J_{\beta_{\text{LE}}} & 0 \\ & \text{sym.} & & J_{\beta_{\text{TE}}} \end{bmatrix} \qquad \mathbf{C}_s = 4\pi\xi\,\text{diag}\left(mf_h, J_\theta f_\theta, 0, 0\right) \qquad \mathbf{K}_s = 4\pi^2\,\text{diag}\left(mf_h^2, J_\theta f_\theta^2, 0, 0\right)$$

m	J_θ	$J_{\beta_{\text{LE}}}$	$J_{\beta_{\text{TE}}}$	$S_{h\theta}$	$S_{h\beta_{\text{LE}}}$	$S_{h\beta_{\text{TE}}}$	f_h	f_θ	ξ	$k_{\beta_{\text{LE}}}$	$k_{\beta_{\text{TE}}}$
[kg]	[kgm^2]	[kgm^2]	[kgm^2]	[kgm]	[kgm]	[kgm]	[Hz]	[Hz]	[-]	[Nm]	[Nm]
43.41	8.14	1.221	1.628	5.43	0.814	1.0853	4.65	9.3	0.001	23330	31107

Table 2: Structural model data

References

Aghababa, M. P. & Aghababa, H. P. (2014), 'Stabilization of gyrostat system with dead-zone nonlinearity in control input', Journal of Vibration and Control 20(15), 2378–2388.

Astolfi, A., Karagiannis, D. & Ortega, R. (2008a), Nonlinear and Adaptive Control with Applications, pp. 91-114, Chap. 5, Springer, New York, NY.

Astolfi, A., Karagiannis, D. & Ortega, R. (2008b), 'Toward Applied Nonlinear Adaptive Control', Annual Reviews in Control 32, 136–148.

Bae, J., Yang, S. & Lee, I. (2002), 'Linear and nonlinear aeroelastic analysis of fighter-type wing with control surface', Journal Of Aircraft 39(4), 697–708.

Boulkroune, A. & M'saad, M. (2012), 'Fuzzy adaptive observer-based projective synchronization for nonlinear systems with input nonlinearity', Journal of Vibration and Control 18(3), 437–450.

Brenner, M. J. (1996), Aeroservoelastic Modeling and Validation of a Thrust-Vectoring F/A-18 Aircraft, Technical report, NASA Technical Paper 3647.

Chen, P. C. & Lee, D. H. (2008), 'Flight-loads effects on horizontal tail free-play-induced limit cycle oscillation', Journal of Aircraft 45(2), 478–485.

Chung-Chun, K., Shuo-Chieh, C. & Yu-Ren, C. (2008), Observer-based robust adaptive fuzzy sliding mode control for unknown nonlinear dynamical systems with dead-zone input, in 'Systems, Man and Cybernetics, 2008. SMC 2008. IEEE International Conference', pp. 950–955.

Conner, M. D., Tang, D. M., Dowell, E. H. & Virgin, L. N. (1997a), Nonlinear aeroelasticity of an airfoil with control surface freeplay, in '35th AIAA, Aerospace Science Meeting and Exhibit, Reno, NV'.

Conner, M., Tang, D., Dowell, E. & Virgin, L. N. (1997b), 'Nonlinear behavior of a typical airfoil section with control surface freeplay: A numerical and experimental study', Journal of Fluids and Structures 11(1), 89–109.

Conner, M., Virgin, L. & Dowell, E. (1996), 'Accurate numerical integration of state-space models for aeroelastic systems with free play', AIAA Journal 34(10), 2202–2205.

Croft, J. (27 August 2001), 'Airbus elevator flutter: annoying or dangerous?', Aviation week and space technology .

Daynes, S., Weaver, P. M. & Potter, K. D. (2009), 'Aeroelastic study of bistable composite airfoils', Journal of Aircraft 46(6), 2169–2174.

Dimitriadis, G. & Cooper, J. E. (2000), 'Characterization of the behaviour of a simple aeroservoelastic system with control nonlinearities', Journal of Fluids and Structures 14(8), 1173–1193.

Drakunov, S. & Utkin, V. (1995), Sliding mode observers. tutorial., in 'Proceedings of the 34th Conference on Decision and Control, IEEE, New Brunswick, NJ', pp. 3376–3378.

Ferretti, G., Magnani, G., Martucci, G., Rocco, P. & Stampacchia, V. (2003), Friction model validation in sliding and presliding regimes with high resolution encoders, in 'Experimental Robotics VIII', Vol. 5 of Springer Tracts in Advanced Robotics, Springer Berlin Heidelberg, pp. 328–337.

Frampton, K. & Clark, R. L. (2000), 'Experiments on control of limit cycle oscillations in a typical section', Journal of Guidance, Control and Dynamics 23(5).

Gold, P. & Karpel, M. (2008), 'Reduced-Size Aeroservoelastic Modeling and Limit-Cycle-Oscillation Simulations with Structurally Nonlinear Actuators', Journal Of Aircraft 45(2), 471–477.

Hall, K., Thomas, J. & Dowell, E. (2000), 'Proper Orthogonal Decomposition Technique for Transonic Unsteady Aerodynamic Flows', AIAA Journal 38(10), 1853–1862.

Haykin, S. (2008), Neural Networks and Learning Machines, Prentice Hall, Upper Saddle River, NJ; 3 edition.

Huang, R., Hu, H. & Zhao, Y. (2013), 'Nonlinear aeroservoelastic analysis of a controlled multiple-actuated-wing model with free-play', Journal of Fluids and Structures 42(October 2013), 245–269.

Johnson, D. R., Harne, R. L. & Wang, K. W. (2014), 'A disturbance cancellation perspective on vibration control using a bistable snap-through attachment', Journal of Vibration and Acoustics 136(3), 031006–031006.

Karpel, M., Shousterman, A., Maderuelo, C. & Climent, H. (2013), Dynamic aeroservoelastic response with nonlinear structural elements, in '54th AIAA, ASME, ASCE, AHS, ASC Structures, Structural Dynamics and Material Conference, Boston, MA'.

Kholodar, D. (2014), 'Nature of Freeplay-Induced Aeroelastic Oscillations', Journal Of Aircraft 51(2).

Lee, K. & Singh, S. N. (2010a), 'Non-Certainty-Equivalent Adaptive Control of a Nonlinear Aeroelastic System', International Journal of Electronics and Telecommunications 56(4), 463–471.

Lee, K. W. & Singh, S. N. (2009), 'Immersion- and Invariance-Based Adaptive Control of a Nonlinear Aeroelastic System', Journal of Guidance, Control and Dynamics 32(4), 1100–1110.

Lee, W. L. & Singh, S. N. (2010b), 'Multi-Input Noncertainty-Equivalent Adaptive Control of an Aeroelastic System', Journal of Guidance, Control and Dynamics 33(5), 1451–1460.

Lucia, D. J., Beran, P. S. & Silva, W. A. (2004), 'Reduced-order modeling: new approaches for computational physics', Progress in Aerospace Sciences 40(1-2), 51–117.

Mannarino, A. (2015), An adaptive compensation strategy of control surfaces free-play, in 'AIAA Guidance, Navigation, and Control Conference, Kissimee, FL', American Institute of Aeronautics and Astronautics.

Mannarino, A. & Mantegazza, P. (2014a), 'Multifidelity control of aeroelastic systems: an immersion and invariance approach', Journal of Guidance, Control and Dynamics 37(5), 1568–1582.

Mannarino, A. & Mantegazza, P. (2014b), 'Nonlinear aeroelastic reduced order modeling by recurrent neural networks', Journal of Fluids and Structures 48(0), 103 – 121.

Marquardt, D. (1963), 'An algorithm for least-squares estimation of nonlinear parameters', Journal of the Society for Industrial and Applied Mathematics 11(2), 431–441.

Nordin, M. & Gutman, P. (2002), 'Controlling mechanical systems with backlash – a survey', Automatica 38(10), 1633 – 1649.

Powell, M. J. D. (2006), The NEWUOA software for unconstrained optimization without derivatives, in 'Nonconvex Optimization and Its Applications, Vol. 83, pp 255-297', Springer US.

Rios, L. M. & Sahinidis, N. V. (2013), 'Derivative-free optimization: a review of algorithms and comparison of software implementations', Journal of Global Optimization 56(3), 1247–1293.

Ripepi, M. & Mantegazza, P. (2013), 'Improved Matrix Fraction Approximation of Aerodynamic Transfer Matrices', AIAA Journal 51(5), 1156–1173.

Romanelli, G., Castellani, M., Mantegazza, P. & Ricci, S. (2012), Coupled CSD/CFD non-linear aeroelastic trim of free-flying flexible aircraft, in '53rd AIAA/ASME/ASCE/AHS/ASC Structures, Structural Dynamics and Materials Conference, Honolulu, HI'.

Romanelli, G., Serioli, E. & Mantegazza, P. (2010), A "Free" Approach to Computational Aeroelasticity, in '48th AIAA Aerospace Sciences Meeting and Exhibit, AIAA Paper 2010-0176, Orlando, FL'.

Selmic, R. & Lewis, F. L. (2000), 'Deadzone Compensation in Motion Control Systems Using Neural Networks', IEEE Transactions on Automatic Control 45(4).

Seo, D. & Akella, M. R. (2008), 'High Performance Spacecraft Attitude-Tracking Control Through Attracting Manifold Design', Journal of Guidance, Control and Dynamics 31(4), 884–891.

Seo, D. & Akella, M. R. (2009), 'Non-Certainty Equivalent Adaptive Control for Robot Manipulator Systems', System and Control Letters 58(4), 304–308.

Slotine, J.-J. E. & Li, W. (1991), Applied Nonlinear Control, Chap. 8, pp. 311-391, Prentice Hall.

Tang, D. M. & Dowell, E. H. (2013), 'Computational/experimental aeroelastic study for a horizontal-tail model with free play', AIAA Journal: devoted to aerospace research and development 51(2), 341–352.

Tao, G. (2003), Adaptive Control Design and Analysis, Chapter 10, Wiley-IEEE Press, 1 edition, Hoboken, NJ.

Van Overschee, P. & De Moor, B. (1994), 'N4SID: Subspace algorithms for the identification of combined deterministic-stochastic systems', Automatica 30(1), 75 – 93. Special issue on statistical signal processing and control.

Vasconcellos, R., Abdelkefi, A., Hajj, M., Almeida, D. & Marques, F. (2014), 'Airfoil control surface discontinuous nonlinearity experimental assessment and numerical model validation', Journal of Vibration and Control .

Waszak, M. R. (1997), Robust Multivariable Flutter Suppression for the Benchmark Active Control Technology (BACT) Wind-Tunnel Model, in '11th Symposium on Structural Dynamics and Control, Blacksburg, VA'.